HHS Public Access

Author manuscript

Neuron. Author manuscript; available in PMC 2024 August 29.

Published in final edited form as:

Neuron. 2024 July 17; 112(14): 2333–2348.e6. doi:10.1016/j.neuron.2024.04.010.

Specialized connectivity of molecular layer interneuron subtypes leads to disinhibition and synchronous inhibition of cerebellar Purkinje cells

Elizabeth P. Lackey[*,1], **Luis Moreira**[*,1], **Aliya Norton**[*,1], **Marie E. Hemelt**[2], **Tomas Osorno**[1], **Tri M. Nguyen**[1,3], **Evan Z. Macosko**[1,4], **Wei-Chung Allen Lee**[1,5], **Court A. Hull**[2], **Wade G. Regehr**[1,6]

[1]Department of Neurobiology, Harvard Medical School, Boston, MA, USA

[2]Department of Neurobiology, Duke University Medical School, Durham, NC, USA

[3]Current address, Zetta AI LLC, USA

[4]Broad Institute of Harvard and MIT, Stanley Center for Psychiatric Research, Cambridge, MA, USA

[5]Kirby Neurobiology Center, Boston Children's Hospital, Harvard Medical School, Boston, MA, USA

Summary

Molecular layer interneurons (MLIs) account for approximately 80% of the inhibitory interneurons in the cerebellar cortex and are vital to cerebellar processing. MLIs are thought to primarily inhibit Purkinje cells (PCs) and suppress the plasticity of synapses onto PCs. MLIs also inhibit, and are electrically coupled to, other MLIs, but the functional significance of these connections is not known. Here we find that two recently recognized MLI subtypes, MLI1 and MLI2, have highly specialized connectivity that allows them to serve distinct functional roles. MLI1s primarily inhibit PCs, are electrically coupled to each other, fire synchronously with other MLI1s on the millisecond time scale *in vivo*, and synchronously pause PC firing. MLI2s are not electrically coupled, they primarily inhibit MLI1s and disinhibit PCs, and are well suited to gating cerebellar-dependent behavior and learning. The synchronous firing of

[6]Senior Author and Lead Contact: wade_regehr@hms.harvard.edu.

[*]these authors contributed equally

Author Contributions

W.G.R., L.M. and E.P.L. conceptualized the project and designed the slice experiments. W.G.R. and W.-C.A.L. conceptualized and designed EM experiments. C.A.H. conceptualized and designed *in vivo* experiments. E.Z.M. provided crucial insights into MLI1s and MLI2s in the initial phase of this project. E.P.L. and L.M. performed slice experiments and analyzed slice data. L.M. made *Nxph1*^{Cre} mice using the BNORC transgenic core. E.P.L. performed smFISH experiments and analyzed smFISH data. T.N. generated the automated segmentations in the serial EM dataset and helped guide EM reconstructions. W.-C.A.L. provided resources and infrastructure for EM reconstructions. A.N. performed EM reconstructions and analyzed the EM data. T.O. used fluorescent fills of MLIs to determine the characteristic morphological features of MLI subtypes that were crucial to identifying them in EM reconstructions. M.E.H. conducted and analyzed *in vivo* experiments. W.G.R. and E.P.L. wrote the paper with input from the other authors. C.A.H. and M.E.H. wrote the initial draft of the text associated with *in vivo* experiments.

Declaration of Interests

Harvard University filed a patent application regarding GridTape (WO2017184621A1) on behalf of the inventors including W.-C.A.L., and negotiated licensing agreements with interested partners. The other authors declare no competing interests.

electrically-coupled MLI1s, and disinhibition provided by MLI2s, require a major reevaluation of cerebellar processing.

Introduction

The cerebellar cortex contributes to diverse behaviors by transforming mossy fiber inputs into predictions in the form of Purkinje cell (PC) outputs, and then refining those predictions [1]. When mossy fibers convey signals from the rest of the brain and spinal cord, they activate granule cells that both directly excite PCs, and disynaptically inhibit PCs by activating MLIs [1,2]. MLIs control calcium signaling in PC dendrites [3,4], prevent the induction of long-term plasticity at granule cell to PC synapses [4], and decrease PC firing [5]. Suppressing MLI firing degrades coordinated movement [6], suppresses learned motor responses [7], impairs cerebellar-dependent motor learning [4,8–11], and impairs reversal learning, novelty seeking and social behaviors [10].

MLIs contribute to cerebellar processing through diverse signaling mechanisms [1,2]. All MLIs make conventional GABAergic synapses [12], but those located near the PC layer also make specialized structures known as pinceaux near the initial segments of PC axons to provide ephaptic inhibition [13,14]. MLIs are electrically coupled to each other [15–17], leading to synchronous MLI firing on the millisecond time scale in brain slice [17,18], but it is not known if MLIs fire synchronously in behaving animals. In addition to inhibiting PCs, MLIs inhibit other MLIs [12], although the role of such inhibition is not known. One intriguing possibility is that MLI-MLI inhibition could implement disinhibition, a powerful circuit motif that is used elsewhere in the brain for computations such as selective gating and gain modulation [19–24]. Behavioral studies suggest that cerebellar-dependent learning is gated by disinhibition of PCs, but the source of such disinhibition has not been identified [25]. Such disinhibition requires a specialized subpopulation of neurons that primarily inhibit other interneurons, and it is not known if such an MLI subpopulation exists. Using snRNA-seq, we recently found that MLIs are comprised of two molecularly distinct subtypes, which we named MLI1 and MLI2, that surprisingly do not correspond to the classic basket cell and stellate cell categories [26]. There are approximately three times as many MLI1s as MLI2s intermingled throughout the molecular layer [26], with a higher density of MLI1s near the PC layer [27]. MLI1 and MLI2 showed intriguing differences, such as in their excitability and expression of *Gjd2* (the gene encoding connexin 36), increasing the computational potential of MLIs, and suggesting that they could contribute to cerebellar processing in unexpected ways.

Here we determine the synaptic connectivity and electrical coupling of MLI1s and MLI2s, how they influence PC firing, and how they fire *in vivo*. We find that MLI1s are electrically coupled to each other, and they primarily inhibit PCs. In contrast, MLI2s are not electrically coupled, and they primarily inhibit MLI1s to disinhibit PCs. *In vivo* recordings suggest that MLI1s fire synchronously and provide precisely timed inhibition to suppress PC firing, whereas MLI2s promote PC firing. We conclude that specialized firing properties, electrical coupling and synaptic targeting allow MLI1 and MLI2 to have opposing influences on the PC outputs of the cerebellar cortex. In support of this conclusion, *in vivo* recordings

show differential MLI1 and MLI2 activity during behavior, and that they exhibit opposite patterns of activity during licking that correspond with periodic PC modulation. These newly revealed circuit motifs greatly expand the computational power of MLIs in cerebellar processing.

Results

Targeting MLI1 and MLI2 subtypes in brain slice recordings

Our initial approach was to use paired recordings in brain slice to characterize the synapses made by MLI1s and MLI2s. It was necessary to discriminate between MLI1 and MLI2 subtypes in order to compare their synaptic connectivity. We explored the possibility of using transgenic mice to label subtypes of MLIs based on the selective expression of *Nxph1* in MLI2s and *Gjd2* in MLI1s [26]. We made an *Nxph1*^{Cre} mouse line to help identify MLI2s (Figure S1a–c) and used *Gjd2-EGFP* mice [28] to help identify MLI1s (Figure S1de). Fluorophore expression was not perfectly restricted to a subtype for either of these mice. In the case of *Nxph1*^{Cre} mice, this could arise from *Cre* expression in common MLI1 and MLI2 progenitors, which is particularly likely because MLI1 and MLI2 subtypes diverge relatively late in development [26]. We found that in *Nxph1*^{Cre} *Ai14* mice and in *Gjd2-EGFP* mice the brightest cells were, respectively, MLI2s and MLI1s. However, because these lines did not cleanly distinguish MLI1s and MLI2s, we ultimately relied on electrophysiological properties to identify MLI subtypes (Figure S2). We restricted our recordings to the inner two-thirds of the molecular layer where the electrical properties of MLI1 and MLI2 are most distinct [26], and we only determined the synaptic connectivity of MLIs that were unambiguously classified. Based on the finding that only MLI1s express *Gjd2* (connexin 36) and have spikelets (the characteristic currents arising from activity in electrically-coupled MLIs), we used spikelets to identify MLI1s, and a lack of spikelets combined with a high input resistance to identify MLI2s (Figure S2a–c). We found that for MLI1s and MLI2s identified by these criteria, MLI1s had smaller Ih, and that their membrane potential decayed more rapidly following an evoked action potential compared to MLI2s (Figure S2d–h).

For a subset of cells (n=16), we also used a whole-cell recording pipette to fluorescently label identified MLIs (Figures 1, S2ij, and 3e). Previous studies found that MLIs have a continuum of morphologies [29]. Most MLIs near the PC layer have a canonical basket cell morphology, with multiple axon collaterals that make a series of synapses around the somata of Purkinje cells, and extend axons to the vicinity of PC axons where they contribute to specialized structures known as pinceaux, whereas MLIs near the top of the molecular layer have a canonical stellate cell morphology and the axons do not contribute to baskets or pinceaux [12]. Some MLIs in the middle of the molecular layer have intermediate morphologies and look like stellate cells with a small number of pinceaux [29]. For MLI subtypes, MLI2s throughout the molecular layer and MLI1s near the top of the molecular layer have stellate cell morphologies, whereas MLI1s near the PC layer have basket cell morphologies [26,27]. These properties are consistent with snRNAseq studies of MLI subtypes that indicate that MLI2s have relatively uniform molecular properties, but MLI1s have a continuum of molecular properties that vary with distance from the molecular layer [26,27]. Fluorescence images of MLI1-PC pairs show an MLI1 near the PC layer that looks like a

classic basket cell with prominent collaterals that contribute to pinceaux (Figure 1b), and an MLI1 further away from the PC layer that looks more like a classic stellate cell, except that it also extends two collaterals to the vicinity of the initial segments of PC axons to contribute to pinceaux (Figure 1a). For MLIs subtyped on the basis of their electrophysiological properties, 10/10 MLI1s had collaterals that contribute to pinceaux (Figures 1ab and S2i). All of these cells were located within 160 μm of the bottom of the PC layer. We did not record from or fluorescently label any MLIs in more distal regions of the molecular layer where both types of MLIs look like classic stellate cells [26,27]. All MLI2s had classic stellate cell morphologies (6/6), and their axons did not contribute to pinceau-like structures below the PC layer (Figures 1gh and S2j).

MLI1s inhibit PCs and MLI2s disinhibit PCs

Paired recordings indicate that MLI1s and MLI2s have very different effects on PCs. An inhibitory postsynaptic current (IPSC) is shown for an MLI1-PC pair (Figure 1c), and the average conductance was 187 ± 31 pS for MLI1-PC pairs (Figure 1d). As MLIs are spontaneously active *in vivo* and in brain slice, we stimulated presynaptic cells five times a second in these experiments. The strengths of MLI1-PC synapses as a function of relative MLI1-PC positions are shown (Figure 1e). MLI1s inhibited 94% of nearby PCs (Figures 1m and S3a–c, 33 of 35), with short latencies (Figure 1n, 1.65 ± 0.07 ms). Spontaneous IPSCs were present at high frequencies in PCs (Figures S3fg and 1f), and MLI1 stimulation evoked large, brief increases in IPSC frequencies in PCs (Figures S3h and 1fo). MLI2s had very different effects on PCs. Rather than evoking an inhibitory outward current, MLI2s evoked an average current that appeared to be inward (excitatory) that was blocked by the $GABA_AR$ antagonist gabazine (Figure 1i–k). Average currents were determined for each MLI2-PC pair, and for 71% of the pairs the current appeared to be inward (Figures 1m and S3de, 15 of 21). The long latencies of these responses (Figure 1n) raised the possibility that MLI2s disinhibit PCs by suppressing spontaneous inhibitory inputs onto PCs, and that MLI2-PC responses reflect a decrease in an outward current. This was confirmed by the observation that evoking a single spike in an MLI2 transiently reduced IPSC frequency in PCs (Figure 1lo). In order to assess the effects of a single MLI spike on IPSCs in a PC, we detected IPSCs, integrated the events, and subtracted the spontaneous events, leaving behind the influence of stimulation (Figure S3hi). A short latency IPSC was detected for 18% of MLI1 spikes on average, when all MLI1-PC pairs including those with no apparent connection were averaged (Figure 1p), and there was considerable variability in the fraction of spikes that evoked an IPSC for different pairs (Figure 1q). This suggests that on average there are many failures at MLI1-PC synapses, but this number should be interpreted cautiously. The high background of spontaneous inputs onto PCs made it difficult to reliably detect all IPSCs, particularly if they were small, so estimates of failure rates based on these experiments must be considered upper bounds (note that successes were determined after subtracting the baseline levels of spontaneous events). Failure rates were likely higher for the 5 Hz stimulation that depressed synapses by approximately 40% compared to responses evoked by unphysiologically low frequency activation. Increases in IPSC frequency were evoked in 80% of MLI1-PC pairs (Figures S3kl and 1o–q, 28 of 35). For 71% of MLI2-PC pairs, IPSCs were suppressed with a long latency (7.82 ± 0.84 ms, n=15) (Figures S3km and 1o–r). These findings indicate that MLI1s inhibit and MLI2s disinhibit most nearby PCs.

MLI2s powerfully inhibit MLI1s

The above observations suggested that MLI2s disinhibit PCs by inhibiting MLI1s. We therefore recorded from pairs of identified MLIs to assess the target dependence of synaptic connections, and we determined the electrical coupling between MLI subtypes. MLI2-MLI1 IPSCs were large and short latency (Figure 2a). MLI2s inhibited a large percentage of nearby MLI1s (80%, 16/20, Figure 2j), and the average peak inhibitory conductance for all cell pairs was 247 ± 63 pS (Figure 2b). MLI1-MLI2 connections were present in 60% (12/20) of the pairs, (Figure 2cj), but they were weak (22.1 ± 7.3 pS, Figure 2d). Weak inhibition was also present in 50% (10/20) of MLI2-MLI2 connections (27.3 ± 9.1 pS, Figure 2efj). Electrical coupling was present in 67% (20/30) of MLI1-MLI1 pairs, but was not observed for any MLI2-MLI1, MLI1-MLI2, and MLI2-MLI2 pairs (Figure 2gk). For electrically-coupled MLI1s, the presynaptic action potential produced a large inward current in target cells that could be isolated by blocking GABAA receptors with gabazine. Synaptic currents were quantified using the gabazine-sensitive component (Figure 2g, *lower*, *black*). Inhibition was present in 39% (7/18) of the MLI1-MLI1 pairs (Figure 2j), but the average conductance was small (50.3 ± 31.5 pS, Figure 2h). The short latencies of all MLI-MLI synaptic connections suggests that they are all direct (Figure 2i). A comparison of the cumulative plots as a function of connection strength (Figure 2j) shows that synapses between all types of MLIs are present, but that MLI2-MLI1 synaptic connections are the most prevalent, and the largest. This is consistent with MLI2s disinhibiting PCs by suppressing MLI1 firing.

Electrical coupling has been shown to promote synchronous firing on the millisecond time scale in many types of neurons [30–32], including MLIs [17,33,34], but the observation that only MLI1-MLI1 pairs are electrically coupled (Figure 2k) suggests that synchronous firing might be restricted to MLI1-MLI1 pairs. We tested this possibility by recording spontaneous spiking from identified MLI-MLI pairs, and found that 6/7 MLI1-MLI1 pairs and 0/8 MLI1-MLI2 pairs fired synchronously on the millisecond time scale (Figure 2ln), whereas 7/8 MLI2s transiently suppressed the firing of nearby MLI1s (Figure 2mn).

Synaptic targets from EM reconstructions

We also used a large-scale EM dataset and serial reconstructions from lobule V of a mouse cerebellum [35,36] to determine MLI connectivity. Our initial challenge was to identify MLI1 and MLI2 subtypes. We began by using an automated method to detect synapses made by MLIs (Figure 3a) [35,37]. MLIs exhibited two distinct connectivity patterns, with 76% (82/108) of MLIs preferentially targeting PCs, and the rest preferentially targeting MLIs (Figure 3a–c). Based on the properties of synaptic connections in our electrophysiological studies (Figs. 1 and 2), we hypothesized that for EM reconstructions, MLI1s preferentially target PCs, and MLI2s preferentially target MLIs. This is supported by four additional observations. First, the percentage of PC-preferring MLIs in our EM data set (76%) is comparable to the percentage of MLI1s in our snRNA-seq study (75.5%, 32,716 MLI1s / 43,324 total MLIs) [26]. Second, we found that all MLIs within 40 μm of the bottom of the PC layer preferentially target PCs (Figure 3ab), and it has been shown previously that essentially all MLIs in this region are MLI1s [27]. Third, PC- and MLI-preferring MLIs differentially contributed to pinceaux (Figure 3d, *left*), as was the case

for electrophysiologically-identified MLI1s and MLI2s (Figure 3d, *right*). We evaluated the axons of 36 PC-preferring and 14 MLI-preferring MLIs to determine if they extended collaterals below the PC layer and contributed to pinceaux (Figure 3d). MLIs were not included if they did not contribute to any pinceau and their axons left the slice between their soma and the PC layer. Throughout the entire molecular layer, no MLI that preferentially targeted MLIs contributed to pinceaux, as for fluorescence images of identified MLI2s (Figure 3d, *right*). In contrast, all PC-targeting MLIs within 160 μm of the bottom PC layer (31/31) contributed to at least one pinceau, with MLIs nearer to the PC layer contributing to more pinceaux (Figure 3d, *left*). This was similar to fluorescence images of identified MLI1s that were all located within 160 μm of the bottom of the PC layer and contributed to pinceaux (Figure 3d, *right*, Figures 1 and S2ij). In general, there were somewhat more contributions to pinceaux for fluorescence images, which may reflect the thicker slices used for acute slices (230 μm vs 49.5 μm for the EM volume) that better preserves the complete axonal arborization. MLIs located near the top of the molecular layer that preferentially targeted PCs did not contribute to any pinceaux (7/7 MLI1s located more than 160 μm from the PC layer). This is consistent with the known properties of MLI1s in the outer part of the molecular layer [26,27]. Lastly, we found that the presence of spines on the somata provides insight into the molecular identity of MLI subtypes. Fluorescence images of electrophysiologically-identified MLIs showed that the cell bodies of MLI1s tend to be spiny (6/6), and those of MLI2s smooth (5/5) (Figure 3e, *left*). We saw similar properties for EM reconstructions of MLIs that preferentially targeted PCs, which were spiny, and those that preferentially targeted MLIs, which were smooth (Figure 3e, *right*). We determined the number of spines on the somata of 66 MLIs, and calculated their total lengths. PC-preferring MLIs had more spines on their somata that had a longer total length (Figure 3f). All smooth MLIs (21/21, total somata spine length < 3 μm) preferentially targeted MLIs, and all spiny MLIs preferentially targeted PCs (40/40, total somata spine length > 7 μm). The total lengths of spines on the somata were intermediate for 20% (12/60) of the MLIs, and 58% of these cells preferentially targeted PCs and the rest preferentially targeted MLIs. This indicates that the spines that protrude from the somata of MLIs provide an additional link between the identities of fluorescently labelled MLI subtypes and MLIs reconstructed from the EM dataset, however, for some MLIs the somata spine length alone is insufficient to determine subtype identity. Thus, based on multiple lines of evidence, we conclude that within the EM data set, the MLIs that preferentially target PCs are MLI1s and those that preferentially target MLIs are MLI2s.

Reconstructions of MLI1s are shown for neurons located in the lower, middle and upper molecular layer, with PC somata shown in grey (Figures 3g and S4). The lowest MLI1 has a typical basket cell morphology, with 14 axon collaterals extending to the initial segments of 11 PC axons. The middle MLI1 extended an axon for 300 μm within a sagittal plane to form a large number of synapses, and also extended collaterals that contributed to three pinceaux. The upper MLI1 had a classical stellate cell appearance and did not contribute to any pinceaux. This cell has an axon collateral that heads towards the PC layer, but it ends without being cut off by the surface of the volume. MLI1s contributed to pinceaux in a graded manner that depended upon the position in the molecular layer (Figure 3d), which is consistent with the observation that MLI1s have molecular properties that continuously vary

with distance from the PC layer [26]. In contrast, all MLI2s, including cells located near the PC layer, had classical stellate cell morphologies, and did not extend axon collaterals below the PC layer to contribute to pinceaux (Figures 3d and S4).

We reconstructed ten MLI1s (Figure 4a) and ten MLI2s (Figure 4b) and their targets (Figures S5 and S6) to quantify the output synapses of MLI1s and MLI2s. All synapses were manually inspected, and target MLIs were categorized as MLI1s and MLI2s, as described above. The 20 cells used for analysis were chosen because it was possible to determine the subtypes of almost all MLI targets, which required that target MLIs had intact somata and partially intact axons. The vast majority of MLI synapses were onto PCs and other MLIs, but we also examined other targets. For the ten MLI1s and the ten MLI2s examined in detail, more than 99.7% of the synapses (2,024/2,025 for MLI1s and 1,067/1,070 for MLI2s) were onto either MLIs or PCs. MLI1s primarily synapsed onto PCs (Figures 4cd and S7a), and MLI2s primarily synapsed onto MLI1s (Figures 4ef and S7b). The spatial locations of synapses made by MLI1s are summarized by displaying the synapse locations relative to the somata (Figure 4c). Most synapses made by MLI1s were located within 200 μm of the somata. Synapses made by MLI2s onto MLI1s were more spatially restricted, and were present at higher densities towards the apex of the lobule (the tip of the lobule furthest away from the cerebellar nuclei) and towards the PC layer (Figure 4e). This arrangement of synapses is consistent with the tendency of MLIs to more strongly inhibit other MLIs below them within the molecular layer [16], but the preferential inhibition of MLI1s towards the apex of the lobule was unexpected, and suggests an interesting spatial component of disinhibition that is not yet understood. The MLI1s made more total synapses, more synapses onto PCs, fewer synapses onto MLI2s and fewer synapses onto MLI1s (Figure 4g, *upper*). Individual MLI1s synapsed onto approximately the same number of neurons as MLI2s, synapsed onto more PCs, fewer MLI1s and fewer MLI2s (Figure 4g, *lower*). We also quantified the number of contacts made by MLIs onto individual cells of each type (Figure 4h). MLI1s made many synapses onto each PC, but there was a wide range in contacts per cell. MLI2-PC connections consisted of a small number of contacts, which is consistent with the connection strengths observed in Figure 1. MLI2s primarily contacted MLI1s, and there was a wide range of connections per cell, whereas MLI→MLI2, MLI1→MLI1 and MLI2→MLI2 connections had very few contacts, in agreement with the connection strengths observed in paired recordings (Figure 2). On average MLI1s made 202 synapses onto 38 cells, with 179 contacts onto an average of 24 PCs, and MLI2s made 107 synapses onto 31 cells, with 84 contacts onto 20 MLI1s. These reconstructions suggest that there is considerable variability in the number of contacts per cell, which is also consistent with our electrophysiological experiments.

MLI subtypes *in vivo*

Determining the activity of MLI1s and MLI2s during behavior promises to provide insight into their different functional roles. Multielectrode probes make it possible to simultaneously record from many MLIs and PCs, but discriminating between MLI1s and MLI2s *in vivo* is challenging. The *Nxph1*^{Cre} line that we made is not sufficiently selective to optically tag MLI2s for *in vivo* identification or for optogenetic studies. Nonetheless, functional connectivity and synchrony measures informed by our slice and EM results allow us to

identify putative MLI1s and MLI2s from *in vivo* recordings (Fig 5a). We then assessed their firing patterns during quiescence and behavior.

Recordings were performed in the lateral cerebellum across lobule simplex and Crus I, which have been implicated in locomotion and licking behavior [38–43]. We recorded using Neuropixels probes from awake mice head-fixed on a freely moving wheel (Figures 5b and S8), and identified 110 PCs based on characteristic complex spike responses (Figure S8b) and 132 MLIs by their firing rates (>4 Hz) and their laminar location (Figure S8cd). Based on an MLI1:MLI2 ratio of 3.5:1, it is estimated that more than 100 of these are MLI1s and the rest are MLI2s. For cross correlograms between nearby MLIs and PCs, 79 MLIs produced a strong (Z-score>4), short latency (<3 ms) decrease in firing rates in at least one nearby PC (Figure 5c). We classified these MLIs as putative MLI1s based on our finding that MLI1-PC synapses are much stronger than MLI2-PC synapses. On average, putative MLI1s were in close proximity (<125 μm) to an average of 4.3 PCs, and strongly inhibited 3.4 of them. Putative MLI1 inhibition of PCs decreased target PC_{SS} firing by an average of 19.1 ± 0.7 sp/s for 1.30 ± 0.06 ms (Figure S8e) with a latency of 0.70 ± 0.04 ms (Figure 5h). This was shorter than the synaptic delays for MLI1-PC paired recordings, which reflects in part the temperature dependence of synaptic delays [44] and the conditions of our paired recordings (32 °C). Of the 72 putative MLI1s that were close (<125 μm) to at least one other MLI, 59 fired synchronously on the millisecond time scale with at least one other MLI (Figure 5d), and these MLI-MLI cross correlograms (Figure 5g) are similar to those observed for MLI1-MLI1 pairs in brain slices (Figure 2ln). On average, putative MLI1s fired synchronously with 1.7 of 4.3 neighboring MLIs (mean increase of 19.0 ± 1.6 sp/s for 3.4 ± 0.3 ms, Figure S8). Of 335 putative MLI1-MLI pairs, 130 fired synchronously on the millisecond time scale, and only five were inhibitory. These findings indicate that a large fraction of MLI1s fire synchronously with each other in awake mice, and that they have the capacity to transiently pause the firing of multiple PCs, which could evoke precisely timed spikes in cerebellar nuclei projection neurons [18,45].

We set out to identify a group of neurons from our pool of MLIs that exhibited features that are characteristic of MLI2s in brain slice experiments. First, MLI2 inhibition of PC simple spiking is rare and weak (Figure 1). Second, MLI2s do not fire synchronously with other MLIs (Figure 2). We identified 9 putative MLI2s that were located in the molecular layer more than 40 μm from the PC layer to avoid Purkinje layer interneurons [36], that did not inhibit PCs (requiring that there be at least three known or suspected PCs within 125 μm), and they did not fire synchronously with any other MLI. Although the yield of putative MLI2s was low as a result of our restrictive selection criteria, we thought it was important to only include MLIs that displayed the most obvious and robust characteristics of MLI2s. Average cross correlograms indicate that putative MLI2s did not inhibit PCs (Figure 5f), as required by our selection criteria, but they inhibited nearby MLIs (Figure 5g), which is consistent with our brain slice experiments (Figure 2). Putative MLI2s inhibited 12/32 nearby MLIs and decreased MLI firing by 11.7 ± 2.2 sp/s for 4.0 ± 0.9 ms (Figure 5g) with a short latency (Figure 5h).

We next investigated additional properties of these putative MLI populations that were not defined by our selection criteria. We found that average baseline firing rates were

significantly higher for MLI1s than MLI2s, but there was some overlap in the firing rates for the two types of MLIs (Figure 5i). These observations are consistent with the MLI1 and MLI2 spontaneous firing rates in brain slice [26]. We also found that the average MLI1 and MLI2 waveforms differed, although overlap in the waveform properties indicated that for individual cells the waveform alone cannot be used to discriminate between MLI1 and MLI2 (Figure 5j).

To further examine these populations, we next tested predictions about the *in vivo* activity of these MLIs based on our *in vitro* recordings. Specifically, we tested for evidence of PC disinhibition when MLI2 firing rates were elevated by measuring the relationships between putative MLI1, MLI2 and PC_{SS} firing rates. First, we determined the 100 ms intervals when MLI1s fired fastest and slowest, and measured the difference in nearby PC_{SS} firing rates for these conditions ($PC_{MLI1fast} - PC_{MLI1slow}$). We repeated this calculation for MLI2 firing ($PC_{MLI2fast} - PC_{MLI2slow}$). This analysis showed that for nearby PCs, $PC_{MLI1fast} - PC_{MLI1slow}$ was slightly elevated (Figure 5m). This reflects the general trend of locomotion to elevate PC, MLI1 and MLI2 firing (Figure 5n). However, $PC_{MLI2fast} - PC_{MLI2slow}$ was elevated to a much larger extent than $PC_{MLI1fast} - PC_{MLI1slow}$, consistent with ML2s disinhibiting PCs *in vivo* (PC_{SS} = 3.88 ± 0.60 sp/s grouped by MLI1 activity, Δ PC_{SS} = 16.1 ± 2.0 sp/s grouped by MLI2 activity, Figure 5k). As a control, we repeated this for MLI-PC pairs with >125 μm separation, and there was no difference between $PC_{MLI1fast} - PC_{MLI1slow}$ and $PC_{MLI2fast} - PC_{MLI2slow}$ (Figure 5l).

We next sought more direct evidence of PC disinhibition by MLI2s. Although the average MLI2- PC_{SS} cross correlogram between all MLI2s and PCs did not reveal disinhibition following single spikes (Figure 5f), we were able to examine rare cases where we simultaneously recorded from an MLI2 that inhibited a nearby MLI1 that in turn inhibited a PC. In these connected triplets, the average MLI2- PC_{SS} cross correlogram showed that a single spike in a putative MLI2 transiently elevated firing in nearby PCs with a time course consistent with disinhibition mediated by a disynaptic connection (Figure 5m). These findings further support our criteria for identifying MLI subtypes, and independently demonstrate that MLI2s can transiently disinhibit PCs *in vivo*.

Having identified these relationships between the firing of MLI1s, MLI2s, and PCs, we next sought to evaluate how these circuit motifs might operate during behavior. MLI and PC_{SS} firing tend to be elevated during locomotion, and return to lower levels during periods of quiescence [7,42](Figure 5n–q). Consistent with the inhibitory role of MLI1s and disinhibitory role of MLI2s, we find that MLI2s increase their firing to a greater extent than MLI1s when PC_{SS} firing goes up (locomotion onset), and MLI2s decrease their firing to a greater extent than MLI1s when PC_{SS} firing goes down (locomotion offset). These findings are also consistent with the enhanced excitability of MLI2s described *in vitro* [26].

Next, we evaluated the firing of MLIs and PCs during licking. PC_{SS} firing is modulated in periodic manner during the lick cycle [46], and recent evidence has implicated the lateral cerebellum in the regulation of lick timing [38–41]. Consistent with their inhibitory role in regulating PCs, we find that the firing rates of MLI1s and connected PCs are modulated oppositely, with MLI1s firing most rapidly when PC_{SS} firing is at its lowest (Figure 5r).

Remarkably, MLI2s connected to nearby by MLI1s also show an opposite relationship, with MLI2s firing at their highest when MLI1s fire least (Figure 5s). Finally, we were able to isolate one connected PC, MLI1 and MLI2 triplet that was modulated by licking. These data reveal a striking relationship, where elevated MLI1 firing coincides with decreased PC_{SS} firing, and elevated MLI2 firing coincides with increased PC_{SS} firing and decreased MLI1 firing (Figure 5t). Together, these results suggest that the unique circuit motifs established by MLI1s and MLI2s likely play a key role in patterning PC_{SS} activity during behavior.

Discussion

Molecular characterization previously established that there are two major subtypes of MLIs [26], but nothing was known about their connectivity or functional roles. It had been tacitly assumed that all MLIs strongly inhibit PCs and weakly inhibit other MLIs [1,2]. We used paired recordings, serial EM reconstructions and *in vivo* recordings in behaving animals to overturn this view, and demonstrate that MLI subtypes are highly specialized to serve distinct roles that shape cerebellar output in two key ways that are vital for behavior and learning. MLI1s primarily inhibit PCs, they are electrically-coupled to each other, fire synchronously on the millisecond time scale, and synchronously inhibit PCs. MLI2s are not electrically coupled, primarily inhibit MLI1s and disinhibit PCs, thereby providing a critical new circuit mechanism for gating PC excitability and plasticity. These circuit revisions open the door for new models of cerebellar function, and hold promise to resolve longstanding debates about how PC firing can be bi-directionally regulated to enable behavior and learning.

MLI1 and MLI2 synaptic connectivity

One of our main findings is that recently described MLI subtypes have distinct synaptic connectivity that makes them suited to serve different functions. Our evidence supporting differential MLI1 and MLI2 connectivity is particularly strong for MLIs in the inner two thirds of the molecular layer. We restricted our paired recordings to the lower two thirds of the molecular layer, and used electrophysiological properties and axonal morphologies to discriminate between subtypes. As we have shown previously, it is difficult to discriminate between MLI subtypes in the outer third of the molecular layer where MLI1s and MLI2s have similar electrophysiological and morphological properties. EM reconstructions established that MLIs had two very different connectivity patterns throughout the molecular layer: most MLIs preferentially targeted PCs, and the rest preferentially targeted MLIs. For MLIs in the inner two thirds of the molecular layer, MLI subtypes were identified in the EM data set based on paired recordings that established that MLI1s preferentially target PCs and MLI2s preferentially target MLIs, and by using the presence of contributions to pinceaux to identify MLI1s, and their absence to identify MLI2s. Lastly, we quantified the spines on MLI somata to aid in the identification of MLI subtypes. For cells in the inner two thirds of the molecular layer, all MLIs with spiny somata preferentially targeted PCs and had pinceaux, whereas MLIs that preferentially targeted other MLIs had smooth somata. Despite the fact that in the distal third of the molecular layer the electrical properties and the axonal arborizations of MLI1s and MLI2s are similar to each other [26,27], and most MLI1s and MLI2s do not contribute to pinceaux, MLIs have two distinct connectivity patterns in

this region, and intermediate connectivity patterns are not apparent. Moreover, when the properties of somatic spines were quantified and compared to the connectivity for cells in the distal molecular layer, all MLIs with very spiny somata preferentially targeted PCs, and all MLIs with smooth somata preferentially targeted MLIs. We therefore conclude that MLI2s throughout the molecular layer preferentially target other MLIs, and even though MLI1s are a continuum with regard to morphological, electrical, and molecular properties, MLI1s throughout the molecular layer preferentially target PCs.

Although both MLI subtypes exhibit differential target-dependent selectivity, they both form at least some synapses onto MLI1s, MLI2s, and PCs. Electrophysiological studies and EM reconstructions established MLI1s primarily inhibit PCs, and weakly inhibit MLI1s and MLI2s, and MLI2s primarily inhibit MLI1s and weakly inhibit PCs and MLI2s. MLI1-MLI2, MLI1-MLI1, MLI2-MLI2, MLI2-PC connections are stronger and more prevalent than the connections between MLIs and Golgi cells, which are exceedingly rare or entirely absent. It seems likely that the weak synapses made by MLI1s and MLI2s onto their secondary targets have functional roles, but further studies are needed to clarify what they are.

MLI2 disinhibition

The discovery that MLI2s are disinhibitory interneurons indicates that the molecular layer of the cerebellum shares a circuit motif that plays an important processing role in many brain regions, including layer 1 of the cerebral cortex [19–24]. Whereas elevated MLI activity suppresses calcium signaling in PC dendrites and suppresses the induction of LTD at granule cell to PC synapses [3,4], the finding that MLI2s inhibit MLI1s suggests that it is possible to bidirectionally influence LTD induction. A recent study implicated a disinhibitory circuit involving MLIs in the cerebellar flocculus in regulating gain increase learning of the vestibular ocular reflex [25]. It seems likely that MLI2s provide the primary source of disinhibition that allows MLIs to gate this form of learning. MLI2s also provide a means of countering granule cell excitation of MLI1s to keep them in a responsive range, and they allow bidirectional regulation of MLI1 firing rates. This also allows flexible and bidirectional regulation of PC firing rates in a manner that could not be readily achieved with a simple feedforward inhibitory circuit where inhibition scales with incoming excitation. Indeed, our *in vivo* recordings suggest that differential MLI1 and MLI2 firing is likely to shape ongoing PC activity during behavior. In particular, the inverse patterns of MLI1 and MLI2 activity during licking suggest a key role for these distinct cell types in shaping ongoing PC_{SS} activity and behavior. In the future, the newfound ability to identify MLI1 and MLI2s *in vivo*, together with technologies such as neuropixels that allow for simultaneous recordings of these cells along with PCs, promises to lead to new insights into the advantages of disinhibition for behavior and learning.

Regarding whether distinctive MLI2 connectivity is present across all regions of the cerebellar cortex, our working hypothesis posits that the regional circuit specializations in the cerebellar cortex primarily stem from variations in mossy fiber inputs and PC outputs, rather than regional disparities in inhibitory interneurons such as MLIs. This is supported by the observation in our snRNAseq studies that PCs exhibit strong regional

specializations, but MLI1s and MLI2s do not [26]. Notably, this contrasts with unipolar brush cells, a type of excitatory interneuron that shows marked regional specializations [47]. Our EM reconstructions were performed in lobule V of the vermis, our paired recordings were made primarily in lobules III-VII of the vermis, and our *in vivo* studies were performed in lobule simplex and Crus I and together they provide a consistent view of MLI connectivity. Behavioral studies that require a disinhibitory circuit involving MLIs to regulate cerebellar dependent plasticity involve the flocculus [25]. Although further studies are required to directly determine the MLI connectivity in other regions of the cerebellar cortex, it seems likely that the specialized connectivity of MLI1s and MLI2s is conserved throughout all regions of the cerebellar cortex.

MLI1 synchrony and PC inhibition

A combination of slice experiments and *in vivo* recordings establishes that selective expression of GJD2 (connexin 36) in MLI1s [26] leads to MLI1-MLI1 pairs that are electrically coupled and fire synchronously with each other on the millisecond time scale, but other combinations of MLIs are not electrically coupled and do not fire synchronously. The putative MLI1-MLI1 cross-correlograms we observed *in vivo* are very similar to those seen for electrically-coupled MLI1-MLI1 pairs in brain slices, suggesting that electrical coupling in MLI1s underlies their synchronous firing *in vivo*. Electrical coupling also allows MLI1s to share charge from synaptic inputs, as has been described for Golgi cells [48], and consequently MLI1s are not completely independent circuit elements. Granule cell excitation of MLI1s can spread to nearby MLI1s as a result of electrical coupling and the depolarizing component of spikelets to promote synchronous MLI1 firing, which in turn allows many MLI1s to simultaneously and precisely inhibit PCs [34]. Transient decreases in PC firing arising from synchronous inhibition from multiple MLI1s are suited to promote precisely-timed increases in firing within cerebellar nuclei [18]. This suggests that MLI1-induced synchronous pauses in PC firing could help gate the output of the cerebellar cortex. EM reconstructions indicate that direct electrical coupling is only possible for MLI1s whose dendrites reside within approximately the same parasagittal plane, making electrical coupling between MLI1s suited to coordinating firing within parasagittal microzones [39,49,50].

The subdivision of a population of interneurons into two subtypes, one that is not electrically coupled that inhibits a second subtype that is electrically coupled, as we show here for MLIs, is a circuit motif that may occur in other populations of interneurons. Our snRNAseq analysis of neurons in the cerebellar cortex suggests that this is also likely the case for Golgi cells, which are subdivided into a large population that expresses GJD2, and a smaller population that does not [26]. Further experiments are required to determine whether the connectivity of Golgi cell subtypes has similar synaptic connectivity to that exhibited by MLIs. There are also subtypes of SST inhibitory interneurons in the cerebral cortex, and intriguingly SST44 subtype interneurons are electrically coupled and fire synchronously to provide an error signal [51]. With so many populations of interneurons electrically coupled throughout the brain, the circuit motif described here for MLI1s and MLI2s may also be present in additional brain regions.

STAR METHODS

RESOURCE AVAILABILITY

Lead contact—Requests for further information, resources, and reagents should be directed to the lead contact, Wade G. Regehr (wade_regehr@hms.harvard.edu).

Materials availability—Mouse lines are either publicly available or will be shared within the limits of existing material transfer agreements.

Data and code availability

- The EM dataset was published [35] and is deposited at the BossDB repository (https://bossdb.org/project/nguyen_thomas2022).
- Software used in this work is available in the repositories listed in the key resources table.
- Any additional information is available from the lead contact upon request.

EXPERIMENTAL MODEL AND STUDY PARTICIPANT DETAILS

Animal procedures were performed in accordance with the NIH and Animal Care and Use Committee (IACUC) guidelines and protocols approved by the Harvard Medical School Standing Committee on Animals. C57BL/6 mice were obtained from Charles River Laboratories. *Gjd2-EGFP* mice were obtained from MMRRC (stock # 030611-UCD) [28]. *Nxph1*^{Cre} mice were crossed with *Ai14* reporter mice (Jackson Labs, stock # 007908) [52] and kept in a mixed genetic background. Animals of either sex were randomly selected for experiments. Animals were housed on a normal light–dark cycle with an ambient temperature of 18–23 °C with 40–60% humidity.

Mice for *in vivo* recordings (15 mice, 8 male, >P55) with a C57 or CBA background (1 C57, 2 C57 x c-Kit Cre, 12 C57 x CBA) were used in accordance with approval from the Duke University Animal Care and Use Committee. Animals were housed on a normal light–dark cycle, and animals of either sex were randomly selected for experiments.

Generation of Nxph1^{Cre} mice—Easi-CRISPR [53] was used to generate the *Nxph1*^{Cre} mouse line, resulting in the insertion of a p2a-Cre recombinase after the *Nxph1* exon 3 stop codon, TGA (Figure S1a). First, CAS9 (PNABio, CP01-50) sgRNA (CCUGUUCAUCUUCAUCCGGA, Synthego) and ssDNA (p2a-Cre cassette flanked by 150 nucleotides homology arms on 5’ and 3’ ends, IDT) were injected in fertilized eggs of FVB mice (Beth Israel Deaconess Medical Center Transgenic Core Facility), then founders carrying the desired insertion were detected through PCR and subsequently sequenced around the insertion to confirm intact cassette sequence (Biopolymers Facility at Harvard Medical School).

HCR-FISH and immunohistochemistry—Based on the selective expression of *Gjd2* in MLI1s and *Nxph1* in MLI2s [26], we hoped that *Gjd2-EGFP* mice and *Nxph1*^{Cre}*Ai14* mice would allow us to target MLI1s and MLI2s, respectively. We used HCR-FISH in

combination with immunohistochemistry to assess the suitability of these mouse lines. Acute cerebellar slices (1 midline slice per mouse) from p28-p45 mice were prepared as described, and fixed for 2 hours in 4% paraformaldehyde in PBS (Biotum) at 4 °C. Slices were stored overnight in 70% ethanol in RNase-free water at 4 °C. A floating slice HCR protocol [26] was performed with the following probes and matching hairpins (Molecular Instruments): sortilin related VPS10 domain containing receptor 3 (*Sorcs3*), and neurexophilin 1 (*Nxph1*). MLI1s express *Sorcs3* and *Gjd2*, MLI2s express *Nxph1*. Amplification hairpins were B1-647 (Alexa 647) and B2-488 (Alexa 488) or B2-594 (Alexa 594) for fluorescence imaging in conjunction with TdT or GFP. Anti-GFP immunohistochemistry was performed between permeabilization and hybridization. Slices were incubated in blocking solution containing primary antibody (chicken anti-GFP, Abcam, 1:1000) overnight at room temperature. Slices were washed in 2x SSC (3 × 5 min) and incubated in blocking solution containing secondary antibody (anti-chicken Alexa 488, Abcam, 1:1500) for 2 hours at room temperature. Slices were washed in 2x SSC (3 × 5 min), postfixed in 4% paraformaldehyde for 10 min, and washed in 2x SSC (3 × 5 min) before hybridization.

Slices were mounted on slides (Superfrost Plus, VWR) with mounting medium (Fluoromount, ThermoFisher) and no.1 coverslips. Images were acquired with a Leica Stellaris X5 confocal microscope using a 63x oil immersion objective (1.4 NA, Olympus). The reporter and HCR probe/hairpin channels were imaged with 180 nm resolution in a 10-20-µm thick, 0.5-µm interval tiled z series in lobule IV/V. Noise was reduced using a median filter with a 2-pixel radius for each focal plane in Fiji (ImageJ). *Sorcs3*+ and *Nxph1*+ cell locations in the molecular layer were manually labelled using the multi-point tool in Fiji. TdT or GFP fluorescence in each cell was averaged within a 7-µm diameter circular mask in Matlab (Mathworks).

TdT labelling was observed in MLIs in $Nxph1^{Cre}Ai14$ mice (Figure S1b). Essentially all MLI2s (*Nxph1*+/*Sorcs3*- cells in the molecular layer) were labelled, and some were very intensely labelled (Figure S1b–c). Approximately 55% of the MLI1s (*Nxph1*-/*Sorcs3*+ cells in the molecular layer) had very low fluorescence levels, and the rest had moderate fluorescence levels. We found that targeting bright cells in $Nxph1^{Cre}Ai14$ mice allowed us to target MLI2s (although we also performed a complete electrophysiological characterization to insure the identity of MLI subtypes). Although $Nxph1^{Cre}$ is useful for identifying MLI2s, it does not provide sufficient selectivity for optogenetic activation or suppression of MLI2s.

We characterized *Gjd2-EGFP* mice in a similar manner, and found many MLIs were labelled in these mice (Figure S1de). Quantification of the GFP fluorescence intensity showed the most MLI2s had low fluorescence levels, but that some were moderately fluorescent. Conversely, some MLI1s had moderate fluorescence levels, but some were very bright. Almost all bright cells were MLI1s. Ultimately, it was not necessary to use *Gjd2-EGFP* mice to identify MLI1s, because most MLIs are MLI1s, and electrophysiological characterization of cells allowed us to readily establish that a cell was an MLI1.

METHOD DETAILS

Slice electrophysiology

Slice preparation: Acute parasagittal slices (230-μm thick) were prepared from p28-45 C57BL/6, *Gjd2-EGFP*, or *Nxph1^{Cre}Ai14* mice. Mice were anaesthetized with an intraperitoneal injection of ketamine (10 mg kg^{-1}) and perfused transcardially with an ice-cold solution containing (in mM): 110 choline chloride, 7 $MgCl_2$, 2.5 KCl, 1.25 NaH_2PO_4, 0.5 $CaCl_2$, 25 glucose, 11.6 sodium ascorbate, 3.1 sodium pyruvate, 25 $NaHCO_3$, equilibrated with 95% O_2 and 5% CO_2. Slices were cut in the same solution, and then transferred to artificial cerebrospinal fluid (ACSF) containing (in mM) 125 NaCl, 26 $NaHCO_3$, 1.25 NaH_2PO_4, 2.5 KCl, 1 $MgCl_2$, 1.5 $CaCl_2$ and 25 glucose equilibrated with 95% O_2 and 5% CO_2. Following incubation at 34 °C for 30 min, the slices were kept up to 6 h at room temperature until recording.

Recordings: MLI-PC and MLI-MLI paired recordings were performed at 32 °C with an internal solution containing (in mM): 150 K-gluconate, 3 KCl, 10 HEPES, 3 MgATP, 0.5 NaGTP, 0.5 EGTA, 5 phosphocreatine-tris$_2$ and 5 phosphocreatine-Na$_2$ (pH adjusted to 7.2 with KOH, osmolarity adjusted to 310 mOsm kg^{-1}). Biocytin (0.2–1%) and Alexa 488 (0.1 mM) were added to the internal solution for MLIs and PCs, respectively. A calculated junction potential of −16.9 mV was corrected. Visually guided whole-cell recordings were obtained with patch pipettes of ~1-3-MΩ resistance for PCs and ~3-6-MΩ resistance for MLIs pulled from borosilicate capillary glass (BF150-86-10, Sutter Instrument). Slice recordings with PC leak currents greater than 500 pA were rejected. Electrophysiology data were acquired using a Multiclamp 700A or 700B amplifier (Axon Instruments), digitized at 20 kHz and filtered at 4 kHz. A subset of recordings was digitized at 100 kHz and down sampled to 20 kHz. Acquisition and analysis of slice electrophysiological data were performed using custom routines written in Igor Pro (Wavemetrics) and Matlab. The following receptor antagonists were added to the ACSF solution to block glutamatergic and glycinergic synaptic currents (in μM): 2 (*R*)-CPP, 5 NBQX, 1 strychnine. The $GABA_AR$ antagonist SR95531 (gabazine, 10 μM) was washed-in for a subset of experiments. All drugs were purchased from Abcam and Tocris.

Recordings were made from the vermis, primarily from lobules III-VII. We recorded from MLIs in the inner two-thirds of the molecular layer and determined the identity of MLI1s and MLI2s by characterizing a number of characteristic electrical properties (Figure S2). It was previously shown that spikelets are present in MLI1s but not in MLI2s, the input resistance is lower in MLI1s, and I_h is larger in MLI2s [26]. MLIs were held at −65 mV in voltage clamp for 30 s to determine if spikelets were present. Recordings were performed deep in slices because the spikelet detection relies on the activity of connected cells. Input resistances (R_i) were determined using a 10 pA, 50 ms hyperpolarizing current step averaged over 50 trials. To activate the hyperpolarization-evoked currents (I_h), MLIs were held at −65 mV and a 30 pA hyperpolarizing current step of 500 ms duration was injected. The amplitude of I_h was calculated as the difference between the maximal current evoked by the hyperpolarizing current step and the average steady-state current at the end (480–500 ms) of the current step. We also found that following action potential stimulation, the membrane potential decayed with a different time course in MLI1s and MLI2s. We imaged MLI

morphology in a subset of MLIs identified on the basis of their electrical properties (see below), and found that 10/10 MLI1s and 0/6 MLI2s had collaterals that extended below the PC cell body layer to contribute to pinceaux. Some experiments were performed using *Nxph1*^{Cre}*Ai14* mice to select MLI2s based on bright TdT fluorescence (Figure S1bc). We then confirmed MLI2 identity with electrical characterization.

To characterize synapses made by MLI1 and MLI2, presynaptic MLI spikes were evoked in whole-cell current clamp with 5 ms current injections at an average of 5 stimuli/s. ISIs were varied using a Gaussian distribution with standard deviation of 25% to prevent entraining firing in spontaneously firing populations of electrically-coupled MLIs. Presynaptic spontaneous MLI firing was suppressed by negative current injection. Postsynaptic responses were recorded in whole-cell mode in voltage clamp at −65 mV for 500 trials. Responses were also recorded at a holding potential of −30 mV for a subset of experiments. All synaptic currents are averages of 500 trials. Spontaneous action potentials from MLI-MLI pairs (within 5 μm of each other in the sagittal plane) were recorded in loose-patch configuration with ACSF-filled electrodes or in current clamp for 5–10 min.

Analysis: Postsynaptic currents were time-locked to the peak of the first derivative of presynaptic evoked spikes and low-pass filtered at 500 Hz. The amplitudes of outward and inward currents were measured as the average of 2–6 ms and 10–15 ms following the evoked spike, respectively (Figure S3ab). Spontaneous and evoked inhibitory events were detected on the first derivative of PC recordings filtered at 200 Hz, with a threshold of 1.5x the standard deviation. The events were integrated, and spontaneous events were subtracted using a linear fit over the 200 ms window before evoked spike onset (Figure S3hi). The remaining change in events was measured as the average of 10–15 ms following the evoked spike (Figure S3jk). Responses were measured relative to baseline averaged 50 ms prior to the evoked spike, and amplitudes at baseline were measured 25 ms prior to the evoked spike. Pairs were determined to be connected if the response z-score was >2. Latency was measured as the half-max time for connected pairs. To calculate $GABA_A$R-mediated synaptic currents in electrically coupled pairs, the average evoked postsynaptic response after gabazine wash-in was subtracted from the average evoked postsynaptic response before the wash-in. Gap junction conductance was calculated as $g_{j12} = 1/R_j = \Delta I_{post} / \Delta V_{pre}$, with ΔI_{post} being the post-synaptic spikelet amplitude and ΔI_{pre} the pre-synaptic evoked spike amplitude [54]. To determine if MLIs fired synchronously, spontaneous action potentials were detected and manually verified for each cell, and cross correlograms and averages of the normalized spike count from −1 ms to 1 ms were calculated [33].

Cell fills: Recorded MLIs and PCs were filled with 0.2–1% biocytin and 0.1 mM Alexa 488, respectively. Patch electrodes were retracted slowly until the cells resealed. Slices were transferred to a well-plate and submerged in 4% paraformaldehyde in PBS (Biotum). Spines were examined in dedicated experiments where MLIs were resealed immediately after cell type identification, within 5 min of recording. Slices were fixed overnight at 4 °C and kept in the dark to preserve Alexa fluorescence in PCs. Slices were washed in PBS (2 × 5 min) and incubated in 0.1% Tween in PBS containing streptavidin Alexa 594 conjugate (ThermoFisher, 1:1500) for 2 hours at room temperature. Slices were washed in PBS (3 × 5

min) and mounted on slides (Superfrost Plus, VWR) with mounting medium (Fluoromount, ThermoFisher) and no.1 coverslips.

Images of MLI-PC pairs were acquired with a Leica Stellaris X5 confocal microscope using a 63x oil immersion objective (1.4 NA, Olympus). The MLI (streptavidin-Alexa 594) and PC (Alexa 488) channels were imaged with 180 nm resolution in a tiled z series with a 0.5-μm interval. Noise was reduced in the PC channel using a median filter with a 4-pixel radius for each focal plane in Fiji (ImageJ). A maximum intensity z projection image was manually thresholded to create a binary image for each channel in Fiji. For MLI cell bodies examined for spines, images were acquired with a Leica SP8X confocal microscope using a 100x oil immersion objective (1.4 NA, Olympus). Cell bodies were imaged with 20 nm resolution and line averaging of 5 in a z series with a 100 nm interval, and the images were deconvolved using Hyugens software.

Serial EM—We previously imaged and aligned a 776 μm X 753 μm X 49.5 μm volume of lobule V of a mouse cerebellum for EM reconstructions comprised of 1176 45-nm thick parasagittal sections [35]. We used automated image segmentation to generate neuron boundaries and automated synapse prediction to infer synaptic connectivity as described previously [35,37]. Automatically predicted synapses were highly accurate (F-score of 0.938) [35]. We used the neuron segmentation and synapse predictions to reconstruct MLIs and analyze their synaptic outputs. Synapses were identified by characteristic ultrastructural features of GABAergic synapses [55], including a synaptic cleft with a flattening of opposed pre- and post-synaptic membranes and clustering of synaptic vesicles near the presynaptic specialization. Synapses were identified for 108 MLIs using automated synapse detection. The cell bodies of these MLIs were located near the middle of the volume, and it was possible to reconstruct dendritic regions of the target cells and their somata. We also quantified the contributions of 54 MLIs to pinceaux to determine if this could be used to discriminate between MLI subtypes. Axonal projections made below the PC layer and proximal to the axon initial segment of a PC were identified as contributing to a pinceaux. MLIs were excluded if no such contribution was observed, but the axon extending towards the PC layer left the volume. The relationship between number of pinceaux and the position of the MLI somata was approximated with a 3rd order polynomial fit to the data for EM reconstructions, and by the same fit scaled by 1.7 for fluorescence images of identified MLI1s. This suggests that more contributions to pinceaux were present for filled cells, which may arise because EM reconstructions could underestimate this value because part of the axonal arborization might leave the volume (which is only ~50 μm thick compared to over 200 μm thick for acute slices). The properties of spines on the somata were characterized for 66 MLIs to determine if spines could be used to identify MLI subtypes. The lengths of all spines protruding from the somata was determined by measuring the distance from the base to the tip, and total length of all spines longer than 0.3 μm was determined for each. Somata were deemed to be smooth if the total spine length was less than 3 μm, and spiny if the total spine length was greater than 7 μm.

Synapses were proofread manually for ten MLI1 and ten MLI2 cells to validate each postsynaptic target using MD-Seg [35].The cell bodies of these MLIs were located near the middle of the volume, and it was possible to reconstruct dendritic regions of the

target cells and their somata to allow subtype determination of most target MLIs (2.3% of synapses were made onto MLIs that could not be categorized because the cell body of the target cell was not contained within the EM series). Synapses were identified by characteristic ultrastructural features of GABAergic synapses [55], including a synaptic cleft with a flattening of apposed pre- and post-synaptic membranes and clustering of synaptic vesicles near the presynaptic specialization. Plots were rotated 5.62 degrees to compensate for tilt of the PC layer in the volume. Of the 2025 synapses made by the ten MLI1s, 19 were onto MLIs whose subtype could not be determined, and there was a single synapse (0.05%, 1/2025 synapse) made onto a dendrite from an interneuron located in the granule cell layer, which could have been a Golgi cell, a globular cell or a Lugaro cell [1]. For the ten MLI2s examined in detail, 99.95% (1067/1070) of the synapses were onto either MLIs or PCs, 50 were onto MLIs whose subtype could not be determined, there were 2 contacts onto candelabrum cells, and there was a single synapse onto a dendrite from an interneuron located in the granule cell layer. These findings are consistent with a previous study that combined optogenetics and electrophysiology and found that MLI to Golgi cell synapses are extremely weak or entirely absent [56], and with the finding that MLI to candelabrum synapses are present but rare [36].

In vivo recordings

Surgical Procedures: Animals underwent a headposting surgery weeks before recording, during which a titanium headpost (HE Palmer) was affixed to the skull and a stainless steel ground screw (F.S. Tools) was inserted over the left cerebellum, both secured with metabond (Parkell). Mice received dexamethasone (3 mg/k, subq) 4–24 hours before surgery and an initial dose of ketamine/xylazine (50 mg/kg and 5 mg/kg, IP) and carprofen (5 mg/kg) 20 min before induction with isoflurane anesthesia. Isoflurane was administered at 1.0–2.0% throughout surgery to maintain appropriate breathing rates and prevent toe pinch response, which were monitored throughout the duration of the surgery. Body temperature was maintained with a heating pad (TC-111 CWE). Mice received bupranex and cefazolin (0.05 mg/kg and 50 mg/kg respectively, subq) twice daily for 48 h after surgery and were monitored daily for 4 days. After 2+ weeks of recovery, mice received dexamethasone (3 mg/k) 4–24 hours before recordings. Craniotomies (approx. 0.5–1.5 mm) were opened on the first day of recording over lobule simplex or Crus I, under 1–2% isoflurane anesthesia, and were sealed between recordings using Qwik-Cast (WPI) covered by Metabond. Craniotomies could be re-opened for subsequent recordings under brief (<30 min) 1–2% isoflurane anesthesia.

In vivo electrophysiology: After recovery from headpost placement, mice were habituated to be head fixed on a freely moving wheel for at least 30 min over 3 days. Mice were given dexamethasone (2 mg/k) 4–24 hours before recording. After the craniotomy was opened, mice were head fixed on the wheel and allowed to recover from anesthesia. Neuropixels 1.0 electrodes were positioned in the right lateral cerebellum between 0–2 mm lateral and 6–7 mm posterior to Bregma. The electrode was lowered at rate of 1–5 mm/sec through the cerebellar cortex to reach a final placement of 1,000 – 2,500 microns into the cortex. Tissue was allowed to relax for 30 minutes and recordings lasted 30–90 min. Mouse movements were recorded with a rotatory encoder (YUMO) attached to the wheel and licking was

monitored with an optical lick sensor (custom). In some experiments, mice were water deprived for 3–7 days before recording and received a water reward every 20–40 sec during recording to facilitate locomotion and licking. All metrics were computed during quiescent periods unless otherwise noted. After the last day of recording, animals were deeply anesthetized with a ketamine/xylazine (350 mg/kg and 35 mg/kg, IP) and perfused for histology. The electrode was coated with dye (DiI, DiO, or DiD) for visualization, and recording locations were verified in most cases with histology post-hoc (Figure S8a). In total, 19 recordings were made in 15 animals, with 132 MLIs recorded from the lateral cerebellum.

Data was recorded with SpikeGLX software (billkarsh.github.io) and potential units were identified using Kilosort 2.0 [57] and manually curated in phy (GitHub - cortex-lab/phy: phy: interactive visualization and manual spike sorting of large-scale ephys data). All units identified here were well-isolated, having <5% refractory period violations in the ACG (auto-correlogram) compared to the baseline firing rate and missing <5% of spikes based on the unit amplitude histogram. Further analysis was carried out using custom Matlab programs. Voltage signals were filtered with a 300 Hz high pass (first order Butterworth) for waveform analysis. One hundred waveforms were extracted for waveform analysis, aligned to the trough, and the resulting average was normalized using a Euclidean norm.

PC and MLI Identification In Vivo: Potential units in any layer were identified using kilosort 2.0, and well-isolated units were manually curated in Phy. To identify PCs, putative simple spikes and complex spikes from the same PC were initially identified based on firing rates and electrode proximity, along with manual inspection of autocorrelograms, selecting for units firing units firing > 45 Hz and 1–2 Hz respectively (Figure S8). Cross-correlograms (CCGs) for such units were visually inspected for a characteristic complex spike pause in the simple spike firing rate. If the suspected SS firing rate dropped to near zero for 4–20 ms after the suspected complex spike, a pair was accepted as a PC. The Phy plugin “Phyllum” was also used to identify potential Cspk/Sspk pairs, but these were also inspected manually as described above. Additional examples of our PC identification procedures are available [58]. We identified 110 well-isolated PCs based on the characteristic complex spike - simple spike pause (Figure S8b).

Our initial step in identifying MLIs was use neuropixel recordings to isolate units located in the molecular layer. We previously gained experience identifying and recording from MLIs by performing opto-tagging experiments [59]. The layer location of the electrode is discernable in real-time to an experienced user, and post-hoc by examining the firing rates of well-isolated units and the location of identified PCs. Using Phylum (https://github.com/phylum-dev/community-extensions), a custom plug-in to phy from the Medina lab at Baylor College of Medicine, we identified the layer location of each well-isolated unit (Figure S8c). Based on snRNAseq [26] and *in situ* studies [36], we estimate that over 97% of neurons in the molecular layer are MLIs, and the rest are primarily candelabrum cells, which are a type of Purkinje layer interneuron (PLI). Candelabrum cells are located within 40 μm of the PC layer, and only rarely and weakly inhibit PCs [36]. It was also important to consider the possibility that in some cases PCs might be mistaken for MLIs. Although spikes in PC dendrites can generate extracellular signals, these “fat spikes” [60] are readily distinguished

from the rapid extracellular signals associated with MLIs. We identified MLIs in two ways. First, units were identified as MLI1s if they fired above 4 Hz and inhibited a complex spike-identified PC with a short latency (<4 ms), and a >4 SD decrease in firing. Suspected PCs for which a complex spike could not be identified could also be mistaken for an MLI, and it is known that PCs inhibit other PCs [61,62]. We tested known and suspected PCs to see if they fulfilled our criteria for MLI identification. While we observed weak PC-PC inhibition between identified or suspected PCs, in the 275 pairs tested we found only one instance in which it exceeded 4 SD. This suggests that our criteria of a >4 SD decrease in firing excludes the vast majority of PCs for which a complex spike could not be identified. Second, MLIs (either MLI1 or MLI2) were identified if they were recorded on electrodes in the molecular layer more than 40 μm from the PC layer (to exclude candelabrum cells and PCs), and had a firing rate above 4 Hz, regardless of whether or not they inhibited a PC (Figure S8).

Rate-corrected cross correlograms for synchrony and inhibition characterization: Synchrony and inhibition were evaluated using rate-corrected cross correlograms [63]. Briefly, two neurons whose firing rates covary due to correlated inputs or state modulation will display lower frequency comodulation that can be visible on a ccg. We control for this possibility by constructing a “null ccg”, computed by assuming a uniform likelihood of spiking between any given pair of spikes in the spike train for one neuron in each pair. This null ccg shows how many spikes are expected at each time point given only the rate of each neuron. Subtracting the null ccg from the standard ccg gives us the rate corrected ccg, showing how many spikes/second are occurring above the expected coincident spikes given the time-varying firing rates of each neuron. This rate-corrected ccg shows the true amount of synchrony (or inhibition) between neurons, irrespective of low frequency comodulation of firing rates. All correlograms were computed using only time periods during the recording when the animal was quiescent (neither moving nor licking unless otherwise noted). Neurons were classified as synchronous when their rate-corrected ccg surpassed 4 SD above baseline at time zero, and as inhibitory when their rate-corrected ccg dipped below 4 SD from baseline between 0 and 4 ms. (For synchrony evaluations baseline was calculated from −20 to −5 ms on the ccg, and for inhibitory evaluations baseline was calculated from −20 to 0 ms on the ccg.)

Licking and locomotion: The onset of licking was defined as a period of at least 1 second with no lick activity detected, followed by at least 3 licks with an interlick interval less than 300 ms. To identify PCs modulated by licking, the firing rates of the PCs were computed around the time of lick onset (−0.2 to 0.4 seconds) and were smoothed with a Savitzky-Golay filter with a window length of 7 ms. Mice lick in bouts at a frequency of around 8 Hz. Therefore, to identify cells that were modulated by the lick cycle, we used a statistical criterion that required cells to be significantly modulated in this frequency range. To select PCs modulated by the lick cycle, we performed a single-sided fast Fourier transform on the PC_{SS} peristimulus-time histogram of spikes collected during lick bouts, and accepted PCs where the amplitude of this transform had a value greater than 10 $spikes^2/s^2$ at 8 Hz. Licking modulated MLIs less strongly than PCs. MLIs modulated by licking were included if more than 5% of the contribution to the fast Fourier transform was at 8 Hz

The onset of locomotion was defined as the beginning of a period of at least 0.5 seconds with a forward speed more than 0.5 cm/s. The offset of locomotion was defined as the beginning of a period of at least 0.5 seconds with a forward speed less than 0.5 cm/s. As the wheel can move as the mouse breathes, even a mouse at rest can show a speed above 0. Firing rates after onset of locomotion or quiescence were normalized to the period −1 to −0.25 seconds before onset.

QUANTIFICATION AND STATISTICAL ANALYSIS

We did not use statistical methods to pre-determine sample sizes. Technical limitations made it only feasible to analyze one mouse for EM analysis in this study. Details of statistical tests for Figure 1 and Figure 2 are summarized in Table 1. Statistical significance was assumed at $p<0.05$, and exact p and n values are stated in the figure legends and Table 1. For *in vivo* recordings, population firing statistics were visualized with violin plots constructed in Matlab (Hoffmann H, 2015: violin.m - Simple violin plot using Matlab default kernel density estimation. INRES (University of Bonn), Katzenburgweg 5, 53115 Germany. hhoffmann@uni-bonn.de). Kernel densities on the same panel were estimated with common bandwidth supported from the minimum-5 to the maximum+5 of the grouped MLI data (assuming normal density). Statistical comparisons of firing rates between cell type populations were performed with a two-sample Kolmogorov-Smirnov test (Matlab). Two-way comparisons of differences in firing rates between states were computed using the Wilcoxon rank sum test (Matlab). Three-way comparisons were done with a Kruskal-Wallis test, with significant outcomes followed by post-hoc analysis performed with Dunn's test (Matlab). Data are reported as mean ± standard error.

Supplementary Material

Refer to Web version on PubMed Central for supplementary material.

Acknowledgements

We thank Shuting Wu, Joon-Hyuk Lee and Vincent Huson for comments on the manuscript. We thank David Herzfeld for analysis assistance with rate corrected CCGs, and Javier F. Medina, Francisco Naveros and Alvaro Sanchez-Lopez for the use of the Phy plugin "Phyllum" to corroborate layer identification for neuropixels recordings. This work was supported by the NIH (R01MH122570 and R35NS097284 to W.G.R., F32NS133036 to E.P.L., R21NS085320 and RF1MH114047 to W.-C.A.L., 1U19MH114821 to E.Z.M., R01NS128054 and R01NS112917 to C.A.H.), the Bertarelli Program in Translational Neuroscience and Neuroengineering, Stanley and Theodora Feldberg Fund, and the Edward R. and Anne G. Lefler Center. Portions of this research were conducted on the O2 High Performance Compute Cluster at Harvard Medical School partially provided through NIH NCRR (1S10RR028832-01) and a Foundry Award for the HMS Connectomics Core. Equipment in the HMS Neurobiology Imaging Facility was used for confocal imaging. We thank Brad Lowell, Daqing Wang and the BNORC transgenic core for help in making $Nxph1^{Cre}$ mice.

References

1. Hull C, and Regehr WG (2022). The Cerebellar Cortex. Annu Rev Neurosci 45, 151–175. 10.1146/annurev-neuro-091421-125115. [PubMed: 35803588]
2. Kim J, and Augustine GJ (2021). Molecular Layer Interneurons: Key Elements of Cerebellar Network Computation and Behavior. Neuroscience 462, 22–35. 10.1016/j.neuroscience.2020.10.008. [PubMed: 33075461]

3. Callaway JC, Lasser-Ross N, and Ross WN (1995). IPSPs strongly inhibit climbing fiber-activated [Ca2+]i increases in the dendrites of cerebellar Purkinje neurons. J Neurosci 15, 2777–2787. 10.1523/JNEUROSCI.15-04-02777.1995. [PubMed: 7722628]
4. Rowan MJM, Bonnan A, Zhang K, Amat SB, Kikuchi C, Taniguchi H, Augustine GJ, and Christie JM (2018). Graded Control of Climbing-Fiber-Mediated Plasticity and Learning by Inhibition in the Cerebellum. Neuron 99, 999–1015 e1016. 10.1016/j.neuron.2018.07.024. [PubMed: 30122378]
5. Arlt C, and Hausser M (2020). Microcircuit Rules Governing Impact of Single Interneurons on Purkinje Cell Output In Vivo. Cell Rep 30, 3020–3035 e3023. 10.1016/j.celrep.2020.02.009. [PubMed: 32130904]
6. Jelitai M, Puggioni P, Ishikawa T, Rinaldi A, and Duguid I (2016). Dendritic excitation-inhibition balance shapes cerebellar output during motor behaviour. Nat Commun 7, 13722. 10.1038/ncomms13722. [PubMed: 27976716]
7. Gaffield MA, and Christie JM (2017). Movement Rate Is Encoded and Influenced by Widespread, Coherent Activity of Cerebellar Molecular Layer Interneurons. J Neurosci 37, 4751–4765. 10.1523/JNEUROSCI.0534-17.2017. [PubMed: 28389475]
8. ten Brinke MM, Boele HJ, Spanke JK, Potters JW, Kornysheva K, Wulff P, AC IJ, Koekkoek SK, and De Zeeuw CI (2015). Evolving Models of Pavlovian Conditioning: Cerebellar Cortical Dynamics in Awake Behaving Mice. Cell Rep 13, 1977–1988. 10.1016/j.celrep.2015.10.057. [PubMed: 26655909]
9. Wulff P, Schonewille M, Renzi M, Viltono L, Sassoe-Pognetto M, Badura A, Gao Z, Hoebeek FE, van Dorp S, Wisden W, et al. (2009). Synaptic inhibition of Purkinje cells mediates consolidation of vestibulo-cerebellar motor learning. Nat Neurosci 12, 1042–1049. 10.1038/nn.2348. [PubMed: 19578381]
10. Badura A, Verpeut JL, Metzger JW, Pereira TD, Pisano TJ, Deverett B, Bakshinskaya DE, and Wang SS (2018). Normal cognitive and social development require posterior cerebellar activity. Elife 7. 10.7554/eLife.36401.
11. Giovannucci A, Badura A, Deverett B, Najafi F, Pereira TD, Gao Z, Ozden I, Kloth AD, Pnevmatikakis E, Paninski L, et al. (2017). Cerebellar granule cells acquire a widespread predictive feedback signal during motor learning. Nat Neurosci 20, 727–734. 10.1038/nn.4531. [PubMed: 28319608]
12. Palay SL, and Chan-Palay V (1974). Cerebellar Cortex: Cytology and Organization (Springer Berlin Heidelberg).
13. Blot A, and Barbour B (2014). Ultra-rapid axon-axon ephaptic inhibition of cerebellar Purkinje cells by the pinceau. Nat Neurosci 17, 289–295. 10.1038/nn.3624. [PubMed: 24413696]
14. Coddington LT, Rudolph S, Vande Lune P, Overstreet-Wadiche L, and Wadiche JI (2013). Spillover-mediated feedforward inhibition functionally segregates interneuron activity. Neuron 78, 1050–1062. 10.1016/j.neuron.2013.04.019. [PubMed: 23707614]
15. Alcami P, and Marty A (2013). Estimating functional connectivity in an electrically coupled interneuron network. Proc Natl Acad Sci U S A 110, E4798–4807. 10.1073/pnas.1310983110. [PubMed: 24248377]
16. Rieubland S, Roth A, and Hausser M (2014). Structured connectivity in cerebellar inhibitory networks. Neuron 81, 913–929. 10.1016/j.neuron.2013.12.029. [PubMed: 24559679]
17. Mann-Metzer P, and Yarom Y (1999). Electrotonic coupling interacts with intrinsic properties to generate synchronized activity in cerebellar networks of inhibitory interneurons. J Neurosci 19, 3298–3306. 10.1523/JNEUROSCI.19-09-03298.1999. [PubMed: 10212289]
18. Han KS, Chen CH, Khan MM, Guo C, and Regehr WG (2020). Climbing fiber synapses rapidly and transiently inhibit neighboring Purkinje cells via ephaptic coupling. Nat Neurosci 23, 1399–1409. 10.1038/s41593-020-0701-z. [PubMed: 32895566]
19. Topolnik L, and Tamboli S (2022). The role of inhibitory circuits in hippocampal memory processing. Nat Rev Neurosci 23, 476–492. 10.1038/s41583-022-00599-0. [PubMed: 35637416]
20. Kullander K, and Topolnik L (2021). Cortical disinhibitory circuits: cell types, connectivity and function. Trends Neurosci 44, 643–657. 10.1016/j.tins.2021.04.009. [PubMed: 34006387]

21. Garcia-Junco-Clemente P, Ikrar T, Tring E, Xu X, Ringach DL, and Trachtenberg JT (2017). An inhibitory pull-push circuit in frontal cortex. Nat Neurosci 20, 389–392. 10.1038/nn.4483. [PubMed: 28114295]
22. Letzkus JJ, Wolff SB, and Luthi A (2015). Disinhibition, a Circuit Mechanism for Associative Learning and Memory. Neuron 88, 264–276. 10.1016/j.neuron.2015.09.024. [PubMed: 26494276]
23. Pi HJ, Hangya B, Kvitsiani D, Sanders JI, Huang ZJ, and Kepecs A (2013). Cortical interneurons that specialize in disinhibitory control. Nature 503, 521–524. 10.1038/nature12676. [PubMed: 24097352]
24. Letzkus JJ, Wolff SB, Meyer EM, Tovote P, Courtin J, Herry C, and Luthi A (2011). A disinhibitory microcircuit for associative fear learning in the auditory cortex. Nature 480, 331–335. 10.1038/nature10674. [PubMed: 22158104]
25. Zhang K, Yang Z, Gaffield MA, Gross GG, Arnold DB, and Christie JM (2023). Molecular layer disinhibition unlocks climbing-fiber-instructed motor learning in the cerebellum. bioRxiv, 2023.2008.2004.552059. 10.1101/2023.08.04.552059.
26. Kozareva V, Martin C, Osorno T, Rudolph S, Guo C, Vanderburg C, Nadaf N, Regev A, Regehr WG, and Macosko E (2021). A transcriptomic atlas of mouse cerebellar cortex comprehensively defines cell types. Nature 598, 214–219. 10.1038/s41586-021-03220-z. [PubMed: 34616064]
27. Wang WX, and Lefebvre JL (2022). Morphological pseudotime ordering and fate mapping reveal diversification of cerebellar inhibitory interneurons. Nat Commun 13, 3433. 10.1038/s41467-022-30977-2. [PubMed: 35701402]
28. Gong S, Zheng C, Doughty ML, Losos K, Didkovsky N, Schambra UB, Nowak NJ, Joyner A, Leblanc G, Hatten ME, and Heintz N (2003). A gene expression atlas of the central nervous system based on bacterial artificial chromosomes. Nature 425, 917–925. 10.1038/nature02033. [PubMed: 14586460]
29. Sultan F, and Bower JM (1998). Quantitative Golgi study of the rat cerebellar molecular layer interneurons using principal component analysis. J Comp Neurol 393, 353–373. [PubMed: 9548555]
30. Connors BW, and Long MA (2004). Electrical synapses in the mammalian brain. Annu Rev Neurosci 27, 393–418. 10.1146/annurev.neuro.26.041002.131128. [PubMed: 15217338]
31. Connors BW (2017). Synchrony and so much more: Diverse roles for electrical synapses in neural circuits. Dev Neurobiol 77, 610–624. 10.1002/dneu.22493. [PubMed: 28245529]
32. Vaughn MJ, and Haas JS (2022). On the Diverse Functions of Electrical Synapses. Front Cell Neurosci 16, 910015. 10.3389/fncel.2022.910015. [PubMed: 35755782]
33. Han KS, Guo C, Chen CH, Witter L, Osorno T, and Regehr WG (2018). Ephaptic Coupling Promotes Synchronous Firing of Cerebellar Purkinje Cells. Neuron 100, 564–578 e563. 10.1016/j.neuron.2018.09.018. [PubMed: 30293822]
34. Hoehne A, McFadden MH, and DiGregorio DA (2020). Feed-forward recruitment of electrical synapses enhances synchronous spiking in the mouse cerebellar cortex. Elife 9. 10.7554/eLife.57344.
35. Nguyen TM, Thomas LA, Rhoades JL, Ricchi I, Yuan XC, Sheridan A, Hildebrand DGC, Funke J, Regehr WG, and Lee WA (2023). Structured cerebellar connectivity supports resilient pattern separation. Nature 613, 543–549. 10.1038/s41586-022-05471-w. [PubMed: 36418404]
36. Osorno T, Rudolph S, Nguyen T, Kozareva V, Nadaf NM, Norton A, Macosko EZ, Lee WA, and Regehr WG (2022). Candelabrum cells are ubiquitous cerebellar cortex interneurons with specialized circuit properties. Nat Neurosci 25, 702–713. 10.1038/s41593-022-01057-x. [PubMed: 35578131]
37. Buhmann J, Sheridan A, Malin-Mayor C, Schlegel P, Gerhard S, Kazimiers T, Krause R, Nguyen TM, Heinrich L, Lee WA, et al. (2021). Automatic detection of synaptic partners in a whole-brain Drosophila electron microscopy data set. Nat Methods 18, 771–774. 10.1038/s41592-021-01183-7. [PubMed: 34168373]
38. Tsutsumi S, Chadney O, Yiu TL, Baumler E, Faraggiana L, Beau M, and Hausser M (2020). Purkinje Cell Activity Determines the Timing of Sensory-Evoked Motor Initiation. Cell Rep 33, 108537. 10.1016/j.celrep.2020.108537. [PubMed: 33357441]

39. Tsutsumi S, Hidaka N, Isomura Y, Matsuzaki M, Sakimura K, Kano M, and Kitamura K (2019). Modular organization of cerebellar climbing fiber inputs during goal-directed behavior. Elife 8. 10.7554/eLife.47021.
40. Gaffield MA, Sauerbrei BA, and Christie JM (2022). Cerebellum encodes and influences the initiation, performance, and termination of discontinuous movements in mice. Elife 11. 10.7554/eLife.71464.
41. Bina L, Romano V, Hoogland TM, Bosman LWJ, and De Zeeuw CI (2021). Purkinje cells translate subjective salience into readiness to act and choice performance. Cell Rep 37, 110116. 10.1016/j.celrep.2021.110116. [PubMed: 34910904]
42. Armstrong DM, and Edgley SA (1984). Discharges of Purkinje cells in the paravermal part of the cerebellar anterior lobe during locomotion in the cat. J Physiol 352, 403–424. 10.1113/jphysiol.1984.sp015300. [PubMed: 6747896]
43. Sarnaik R, and Raman IM (2018). Control of voluntary and optogenetically perturbed locomotion by spike rate and timing of neurons of the mouse cerebellar nuclei. Elife 7. 10.7554/eLife.29546.
44. Sabatini BL, and Regehr WG (1999). Timing of synaptic transmission. Annu Rev Physiol 61, 521–542. 10.1146/annurev.physiol.61.1.521. [PubMed: 10099700]
45. Heiney SA, Kim J, Augustine GJ, and Medina JF (2014). Precise control of movement kinematics by optogenetic inhibition of Purkinje cell activity. J Neurosci 34, 2321–2330. 10.1523/JNEUROSCI.4547-13.2014. [PubMed: 24501371]
46. Bryant JL, Boughter JD, Gong S, LeDoux MS, and Heck DH (2010). Cerebellar cortical output encodes temporal aspects of rhythmic licking movements and is necessary for normal licking frequency. Eur J Neurosci 32, 41–52. 10.1111/j.1460-9568.2010.07244.x. [PubMed: 20597972]
47. Mugnaini E, Sekerkova G, and Martina M (2011). The unipolar brush cell: a remarkable neuron finally receiving deserved attention. Brain Res Rev 66, 220–245. 10.1016/j.brainresrev.2010.10.001. [PubMed: 20937306]
48. Vervaeke K, Lorincz A, Nusser Z, and Silver RA (2012). Gap junctions compensate for sublinear dendritic integration in an inhibitory network. Science 335, 1624–1628. 10.1126/science.1215101. [PubMed: 22403180]
49. Heffley W, Song EY, Xu Z, Taylor BN, Hughes MA, McKinney A, Joshua M, and Hull C (2018). Coordinated cerebellar climbing fiber activity signals learned sensorimotor predictions. Nat Neurosci 21, 1431–1441. 10.1038/s41593-018-0228-8. [PubMed: 30224805]
50. Kostadinov D, Beau M, Blanco-Pozo M, and Hausser M (2019). Predictive and reactive reward signals conveyed by climbing fiber inputs to cerebellar Purkinje cells. Nat Neurosci 22, 950–962. 10.1038/s41593-019-0381-8. [PubMed: 31036947]
51. Green J, Bruno CA, Traunmuller L, Ding J, Hrvatin S, Wilson DE, Khodadad T, Samuels J, Greenberg ME, and Harvey CD (2023). A cell-type-specific error-correction signal in the posterior parietal cortex. Nature 620, 366–373. 10.1038/s41586-023-06357-1. [PubMed: 37468637]
52. Madisen L, Zwingman TA, Sunkin SM, Oh SW, Zariwala HA, Gu H, Ng LL, Palmiter RD, Hawrylycz MJ, Jones AR, et al. (2010). A robust and high-throughput Cre reporting and characterization system for the whole mouse brain. Nat Neurosci 13, 133–140. 10.1038/nn.2467. [PubMed: 20023653]
53. Miura H, Quadros RM, Gurumurthy CB, and Ohtsuka M (2018). Easi-CRISPR for creating knock-in and conditional knockout mouse models using long ssDNA donors. Nat Protoc 13, 195–215. 10.1038/nprot.2017.153. [PubMed: 29266098]
54. Welzel G, and Schuster S (2019). A Direct Comparison of Different Measures for the Strength of Electrical Synapses. Front Cell Neurosci 13, 43. 10.3389/fncel.2019.00043. [PubMed: 30809130]
55. Peters A, Palay SL, and Webster H.d. (1991). The fine structure of the nervous system : neurons and their supporting cells, 3rd Edition (Oxford University Press).
56. Hull C, and Regehr WG (2012). Identification of an inhibitory circuit that regulates cerebellar Golgi cell activity. Neuron 73, 149–158. 10.1016/j.neuron.2011.10.030. [PubMed: 22243753]
57. Pachitariu M, Sridhar S, and Stringer C (2023). Solving the spike sorting problem with Kilosort. bioRxiv, 2023.2001.2007.523036. 10.1101/2023.01.07.523036.
58. Beau M, Herzfeld DJ, Naveros F, Hemelt ME, D'Agostino F, Oostland M, Sánchez-López A, Chung YY, Maibach M, Stabb HN, et al. (2024). A deep-learning strategy to identify cell

types across species from high-density extracellular recordings. bioRxiv, 2024.2001.2030.577845. 10.1101/2024.01.30.577845.

59. Beau MJR, NAVEROS F, HEMELT ME, OOSTLAND M, SÁNCHEZ LÓPEZ A, Herzfeld DJ, Kostadinov D, Ohmae S, HALL JN, CHUNG Y, et al. (2022). The C4 Initiative: Cross-Species Cell Type Classification Of High-Density Recordings In The Cerebellar Cortex. Program No. 299.04. 2022 Neuroscience Meeting Planner. San Diego, CA: Society for Neuroscience. .
60. Gao H, Solages C, and Lena C (2012). Tetrode recordings in the cerebellar cortex. J Physiol Paris 106, 128–136. 10.1016/j.jphysparis.2011.10.005. [PubMed: 22057014]
61. Witter L, Rudolph S, Pressler RT, Lahlaf SI, and Regehr WG (2016). Purkinje Cell Collaterals Enable Output Signals from the Cerebellar Cortex to Feed Back to Purkinje Cells and Interneurons. Neuron 91, 312–319. 10.1016/j.neuron.2016.05.037. [PubMed: 27346533]
62. Orduz D, and Llano I (2007). Recurrent axon collaterals underlie facilitating synapses between cerebellar Purkinje cells. Proc Natl Acad Sci U S A 104, 17831–17836. 10.1073/pnas.0707489104. [PubMed: 17965230]
63. Herzfeld DJ, Joshua M, and Lisberger SG (2023). Rate versus synchrony codes for cerebellar control of motor behavior. Neuron 111, 2448–2460 e2446. 10.1016/j.neuron.2023.07.002. [PubMed: 37536289]

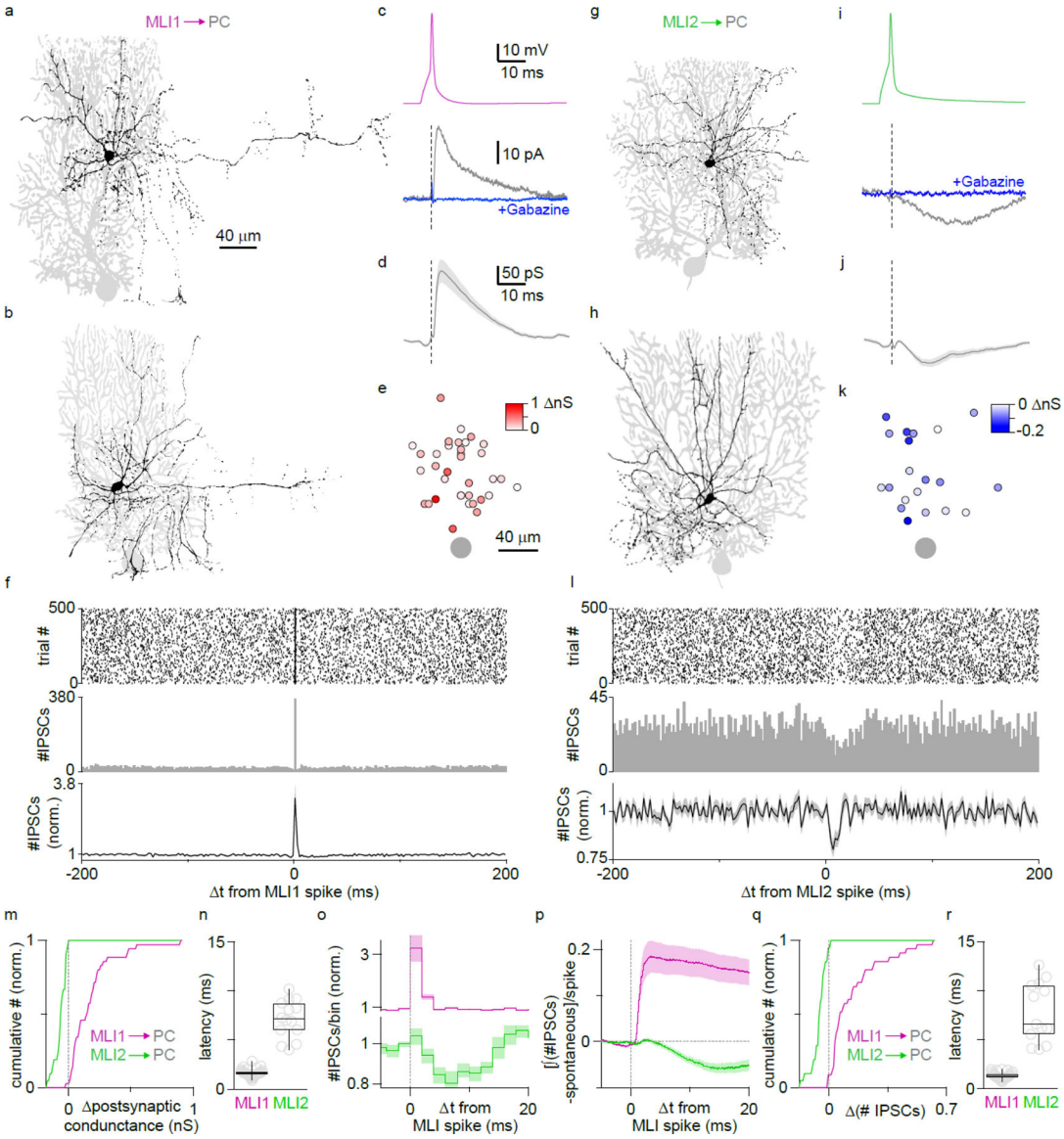

Figure 1. MLI1s inhibit Purkinje cells and MLI2s disinhibit Purkinje cells

Paired recordings between MLIs and PCs were performed, with the presynaptic MLI in current clamp and the synaptic responses in PCs measured in voltage clamp.

a. Fluorescence image of an MLI1 located in the middle of the molecular layer (black) and PC (grey) pair. Scale bar also applies to **bgh**.

b. Same as **a** but for an MLI1 located in the lower molecular layer.

c. Paired recording from an MLI1 (purple) to PC (grey) pair. The $GABA_AR$ antagonist gabazine eliminated the synaptic response (*blue*). Scale bars also apply to **i**. Traces are averages of 500 trials, as is the case for all synaptic currents in Figure 1 and Figure 2.

d. Average MLI1-PC synaptic currents. Scale bars also apply to **j**.

e. Position of MLI1s relative to PCs color-coded for IPSC strength for all pairs.

f. Raster plot of IPSCs (*top*) and corresponding histogram of IPSCs (*middle*) for an MLI1-PC cell pair, and average of histograms (*bottom*) for all MLI1-PC cell pairs.

g-l. Same as **a-f** but for MLI2s.

m. Cumulative plot of amplitudes of all MLI1-PC (*purple*, n=35, p=1E-10) and MLI2-PC (*green*, n=21, p=3E-09) synaptic responses.

n. Latencies of synaptic responses.

o. Expanded histograms from **f** (*upper*) and **l** (*lower*).

p. Average change in the integrated number of IPSCs per spike for all MLI-PC pairs.

q. Cumulative plot summarizing the integrated number of IPSCs per stimulus for all pairs (p=9E-11).

r. Latencies of change in integrated number of IPSCs per spike. See Figure S3 for details on analysis.

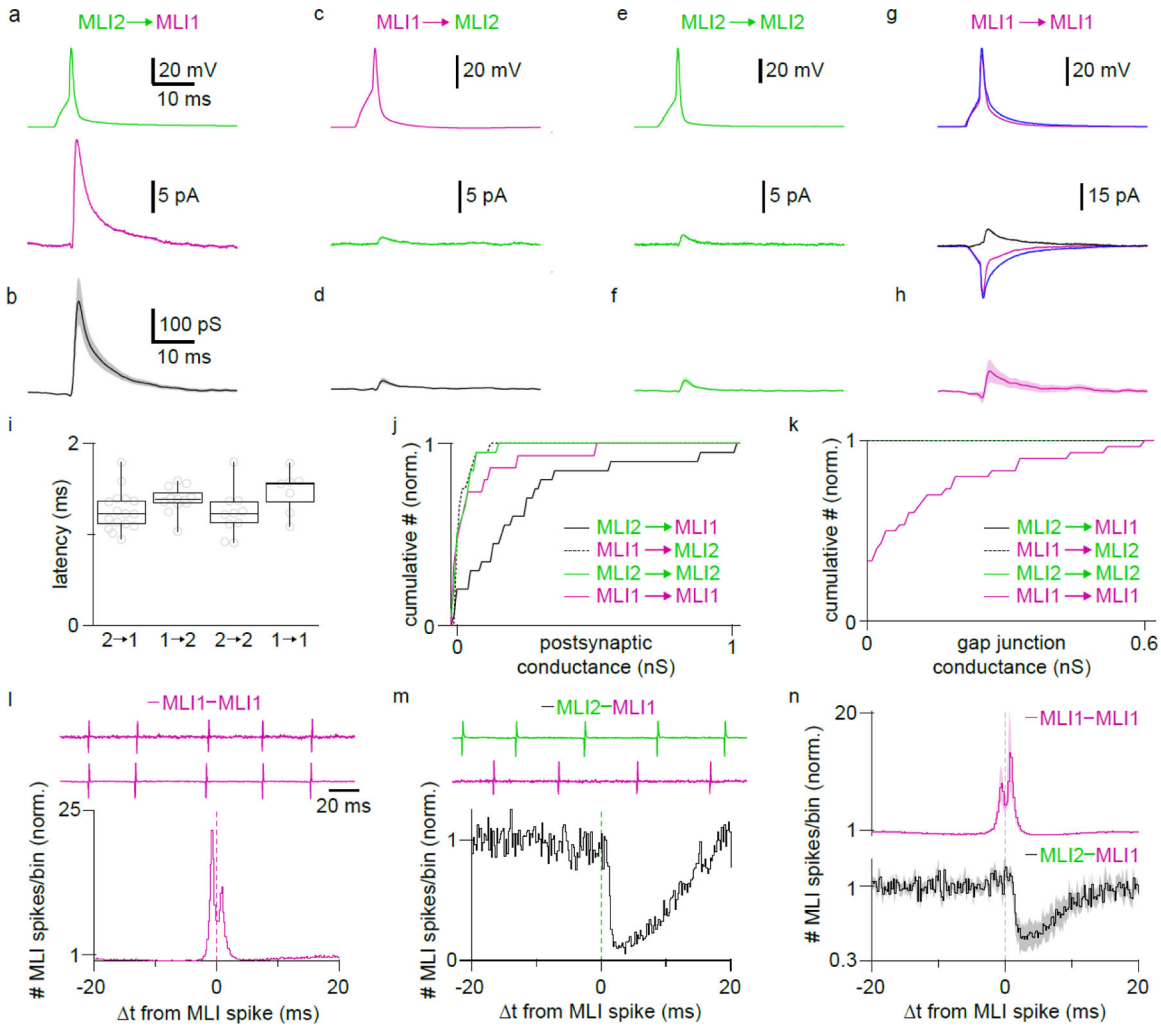

Figure 2. Synaptic connections and electrical connections for MLI-MLI pairs

a. A paired recording with an action potential evoked in a presynaptic MLI2 (current clamp) and the resulting IPSC recorded in an MLI1 (voltage clamp).

b. Average synaptic current for MLI2-MLI1 pairs (n=20, p=2E-08).

c, d). Same as **a, b**, but for MLI1-MLI2 pairs (n=20, p=0.00037).

e, f). Same as **a, b**, but for MLI2-MLI2 pairs (n=20, p=0.0029)

g, h) Same as **a, b**, but for MLI1-MLI1 pairs (n=18, p=0.87). The $GABA_AR$ antagonist gabazine was washed in (*blue*) and the difference between responses evoked in the presence and absence of gabazine are shown (*black*).

i. Summary of latencies for MLI-MLI connections.

j. Normalized cumulative plot of inhibitory conductances for all pairs of MLIs.

k. Normalized cumulative plot of gap junction conductances for all pairs of MLIs.

l. Cross-correlogram of an MLI1-MLI1 pair with on-cell recordings shown above.

m. As in **l**, but for an MLI2-MLI1 pair.

n. Average cross correlograms for MLI1-MLI1 and MLI2-MLI1 pairs. Synchrony was measured as the average normalized spike count from −1 ms to +1 ms (MLI1-MLI1 n=7, p=6E-04; MLI2-MLI1 n=8, p=0.65).

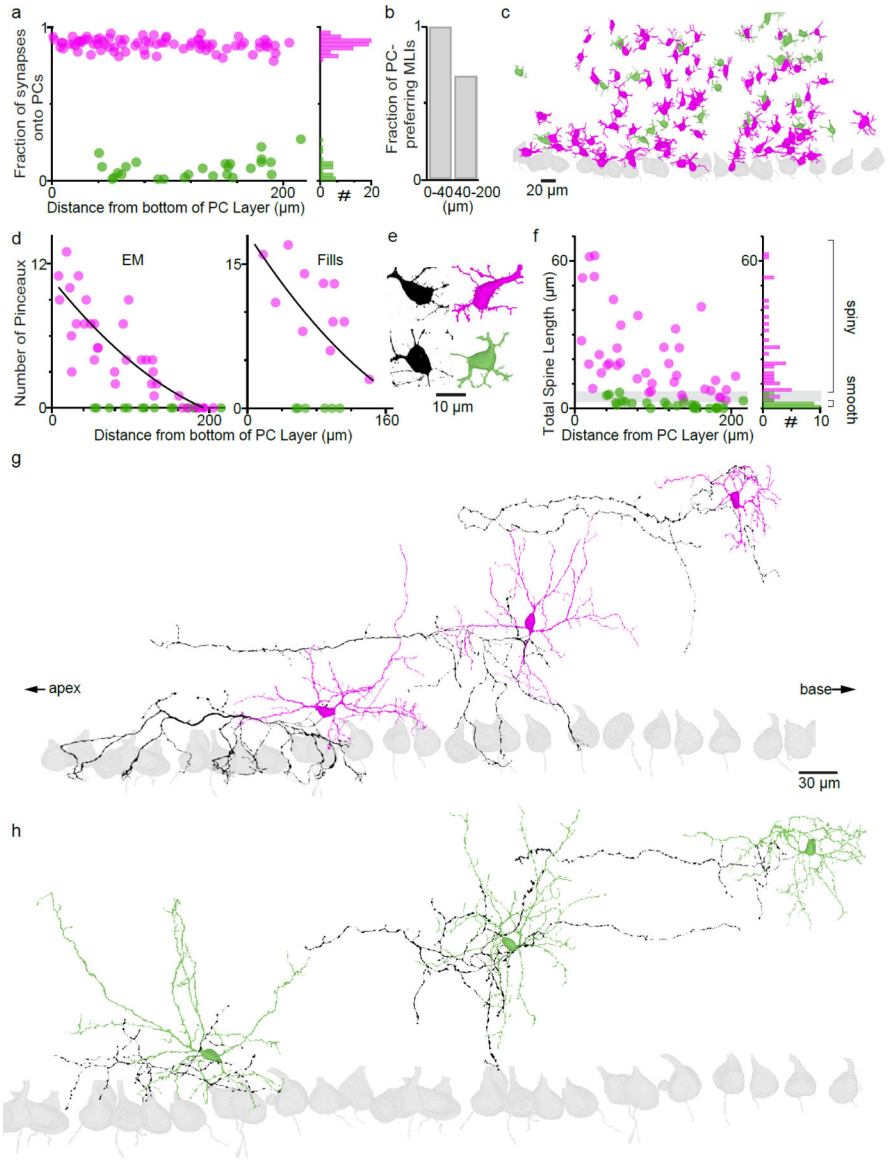

Figure 3. Serial EM reconstructions of MLIs

a. EM reconstructions of MLIs were used to determine the targets of MLIs. The vast majority of synapses were made onto MLIs and PCs.

(*left*) The fraction of synapses made onto PCs was plotted as a function of the distance of the MLI cell body from the bottom of the PC layer. MLIs either preferentially targeted PCs (*purple*) or MLIs (*green*). (*right*) These data are also summarized with a histogram plotted as a function of position in the molecular layer.

b. The fraction of MLIs that preferentially target PCs is plotted for a region near the PCs that has been shown to be strongly enriched for MLI1s (22/22) [27], and for the rest of the molecular layer where MLI1s and MLI2s intermingle (60/86) [26].

c. The somata of the MLIs whose connectivities are summarized in **a** are shown along with PC somata (gre*y*) to illustrate the position of the PC layer.

d. (*left*) Summary of the number of pinceaux for MLIs at different distances from the PC layer for EM reconstructions of MLIs that preferentially target PCs (*purple*) or MLIs (*green*).
(*right*) The number of pinceaux for fluorescently labelled MLI1s (*purple*) and MLI2s (*green*) as in Figure 1.
e. (*top left*) Image of the cell body of a fluorescently labelled MLI1.
(*top right*) EM reconstruction of the cell body of an MLI that preferentially targets PCs (*purple*).
(*bottom left*) Image of the cell body of a fluorescently labelled MLI2.
(*top right*) EM reconstruction of the cell body of an MLI that preferentially targets MLIs (*green*).
f. (*left*) The total lengths of the spines on the somata of MLIs were determined and plotted as a function of the distance of the cell bodies from the bottom of the PC layer.
(*right*) These data are also summarized with a histogram. All spiny MLIs that had a large total spine length were MLI1s, all smooth MLIs that had a small total spine length were MLI2s, and MLIs with intermediate spine lengths were either MLI1s or MLIs (*grey region*).
g. Reconstructed MLIs that preferentially target PCs (MLI1s) are shown, with dendrites (*purple*), and axons (*dark purple*) displayed in different colors. Apex refers to the tip of the lobule furthest away from the cerebellar nuclei, and base refers to base of the lobule closest to the cerebellar nuclei.
h. Reconstructed MLIs that preferentially target MLIs (MLI2s) are shown, with dendrites (*green*), and axons (*dark green*) displayed in different colors.

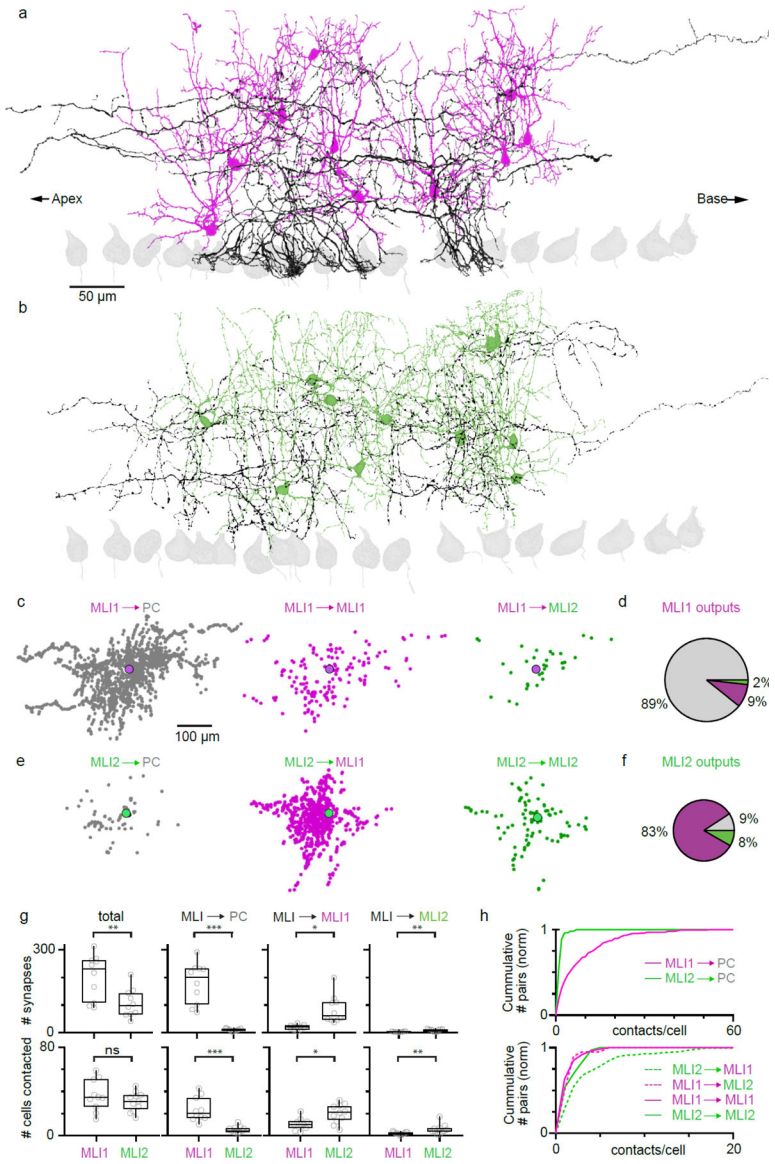

Figure 4. Target-dependence of synaptic connections made by MLI1s and MLI2s determined with serial EM reconstructions

a. Image of 10 reconstructed MLI1s.

b. Image of 10 reconstructed MLI2s.

c. (*left*) Positions of synaptic contacts made by MLI1s onto PCs relative to the MLI1 cell body.

(*middle*) Positions of MLI1 to MLI1 synapses.

(*right*) Positions of MLI1 to MLI2 synapses.

d. Pie chart summarizing synaptic connections made by MLI1s onto different targets.

e. As in (**c**) but for MLI2 synapses.

f. As in (**d**) but for MLI2 synapses.

g. (*top*) Summary of the total number of synapses and the number of synapses onto each type of target made by each MLI and MLI2.

(*bottom*) Summary of the total number of cells contacted and the number of cells targeted by each MLI and MLI2.

h. (*top*) Normalized cumulative plots of the number of synaptic contacts made by individual MLI1s and MLI2s onto PCs.

(*bottom*) Normalized cumulative plots of the number of synaptic contacts made by individual MLI1s and MLI2s onto different types of MLIs.

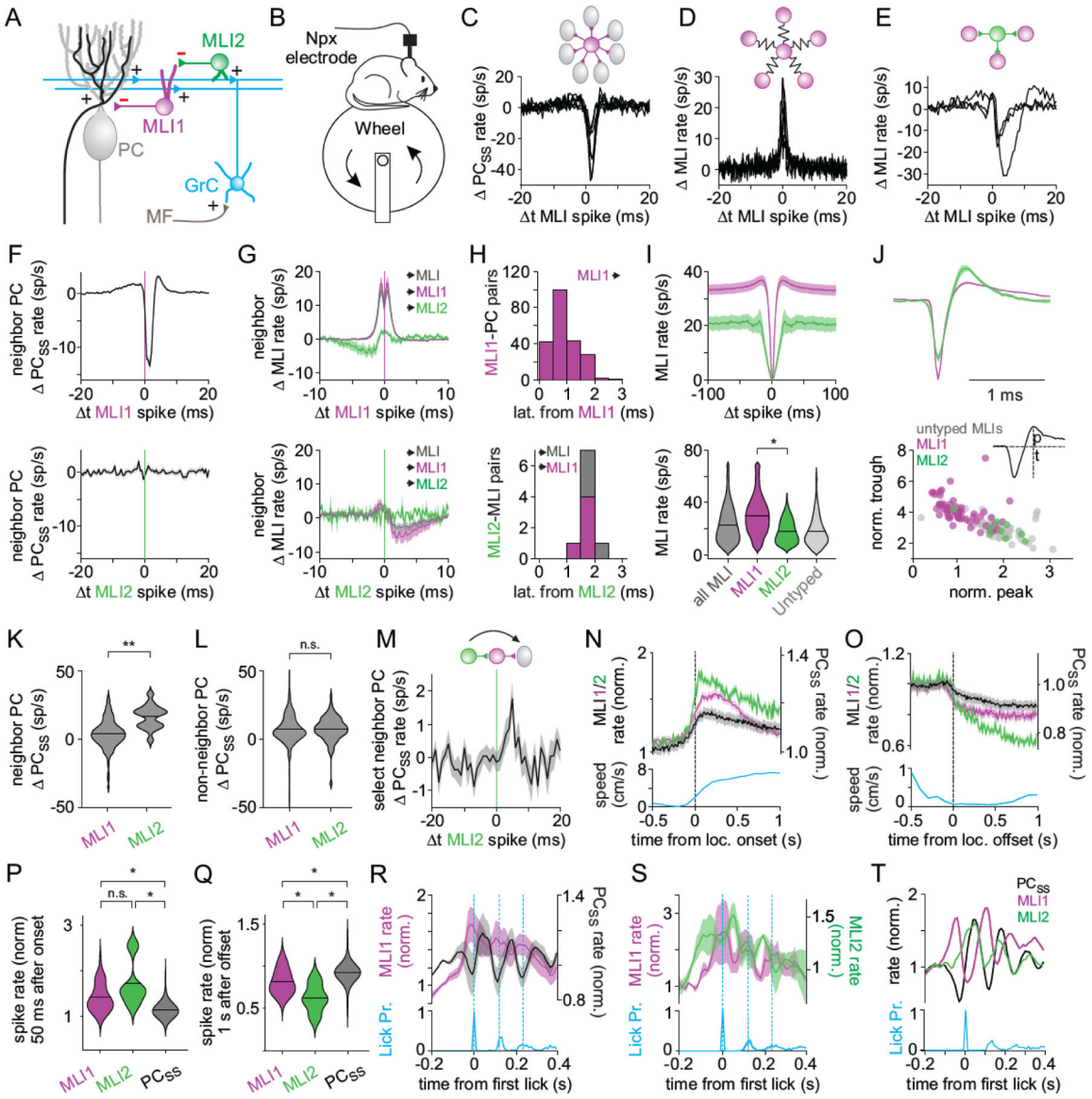

Figure 5. ***In vivo*** **recordings of MLI activity in behaving mice**

a. Schematic of the cerebellar cortex, including MLI1 and MLI2.

b. Neuropixels probes were used to record single-unit activity from the cerebellar cortex of awake mice head-fixed on a freely moving wheel and the properties of neighboring MLIs and PCs (<125 μm separation) were analyzed.

c. An MLI inhibits seven PCs.

d. An MLI fires synchronously with six MLIs.

e. An MLI inhibits 3 MLIs.

f. PCs are inhibited by putative MLI1s but not by putative MLI2s (338 putMLI1-PC pairs; 19 putMLI2-PC pairs).

g. Putative MLI1s fire synchronously with other nearby MLIs (top, 335 MLI1-MLI pairs and 286 MLI1-MLI1 pairs). Putative MLI2s inhibit other MLIs (bottom, 32 MLI2-MLI pairs, 15 MLI2-MLI1 pairs, and 2 MLI2-MLI2 pairs).

h. Latencies of putative MLI1-PC inhibition (top) and from MLI2s onto MLIs (bottom). MLI1, pink; all MLIs, gray.

i. Autocorrelograms and firing rates during quiescence for all MLIs, MLI1s, MLI2s, and unclassified MLIs ($p = 0.012$, 59 putative MLI1s and 9 putative MLI2s).

j. Putative MLI1 and MLI2 mean waveforms (top) and distributions of waveform trough and peak sizes for individual MLIs. (bottom).

k. Difference in PC_{SS} firing rate between periods when neighbor MLI activity was high or low, for MLIs of each type ($p = 0.00002$, MLI1: n = 268 pairs, MLI2: n = 17 pairs).

l. Difference in PC_{SS} firing rate between periods when non-neighbor MLI activity was high or low, for MLIs of each type ($p = 0.36$, MLI1: n = 674 pairs, MLI2: n = 89 pairs).

m. Increase in PC_{SS} rate after MLI2 spikes for simultaneously recorded MLI2-MLI1-PC connections (16 pairs).

n. Firing rates aligned to locomotion onset for MLI1, MLI2, and PC_{SS} (top), and locomotion speed (below), for units that increase firing at locomotion onset (60/110 PC_{SS}, 45/59 MLI1, 9/9 MLI2). A small minority of PC_{SS} decreased firing at locomotion onset (n = 10, not shown).

o. Firing rates aligned to locomotion offset for the MLI1, MLI2, and PC_{SS} shown in n (top), and locomotion speed (below).

p. Normalized firing rates of the MLI1s, MLI2s, and PC_{SS} from n during the first 50 ms of locomotion (MLI1-MLI2 $p = 0.28$, MLI1-PC_{SS} $p < 0.0001$, MLI2-PC_{SS} $p < 0.0001$).

q. Normalized firing rates of the MLI1s, MLI2s, and PC_{SS} from n at 1 sec after locomotion (MLI1-MLI2 $p = .03$, MLI1-PC_{SS} $p = 0.0002$, MLI2- PC_{SS} $p < 0$ .0001).

r. Top: Mean firing rate of connected PCs and MLI1s for PC_{SS} modulated by licking, aligned to lick onset. PC: black, n = 11, MLI1: purple, n = 22. Bottom: Lick probability around the onset of licking.

s. Top: Mean firing rate of connected MLI1s and MLI2s for MLI2s modulated by licking, aligned to lick onset. MLI1: purple, n = 3, MLI2: green, n = 3. Bottom: Lick probability.

t. Top: PC_{SS} rate modulated by licking, together with a simultaneously recorded MLI1 that inhibits this PC, and a simultaneously recorded MLI2 that inhibits this MLI1, all aligned to the onset of licking. PC: black, MLI1: pink, MLI2: green (n=1 simultaneously recorded functionally connected triplet). Bottom: Lick probability.

Table 1.

Summary and statistics of slice electrophysiology experiments

Figure	Group	ΔPostsynaptic Conductance (pS)	SEM (pS)	n	Test	P-Value	Latency (ms)	SEM (ms)	n
Figure 1m,n	MLI1→PC (2–4 ms)	187	31	35	Wilcoxon	1E-10	1.65	0.07	33
	MLI2→PC (2–4 ms)	−4.07	3.96	21	Wilcoxon	0.53			
	MLI1→PC vs MLI2→PC (2–4 ms)				Wilcoxon	9E-11			
	MLI1→PC (10–15 ms)	125	20	35	Wilcoxon	1E-10			
	MLI2→PC (10–15 ms)	−56.2	9.8	21	Wilcoxon	3E-09	7.14	0.52	15
	MLI1→PC vs MLI2→PC (10–15 ms)				Wilcoxon	9E-11			
Figure 2i,j	MLI2→MLI1	247	63	20	Wilcoxon	2E-08	1.26	0.05	16
	MLI1→MLI2	22.1	7.3	20	Wilcoxon	0.00037	1.38	0.04	12
	MLI2→MLI2	27.3	9.1	20	Wilcoxon	0.0029	1.23	0.08	10
	MLI1→MLI1	50.3	31.5	18	Wilcoxon	0.87	1.47	0.09	7
	MLI2→MLI1 vs MLI1→MLI2				Wilcoxon	0.00047			
	MLI2→MLI1 vs MLI2→MLI2				Wilcoxon	0.00037			
	MLI2→MLI1 vs MLI1→MLI1				Wilcoxon	0.0005			
	MLI1→MLI2 vs MLI2→MLI2				Wilcoxon	0.95			
	MLI1→MLI2 vs MLI1→MLI1				Wilcoxon	0.29			
	MLI2→MLI2 vs MLI1→MLI1				Wilcoxon	0.29			
Figure 1o–r	**Group**	**Δ(#IPSCs)**	**SEM (Δ(#IPSCs))**	**n**	**Test**	**P-Value**	**Latency (ms)**	**SEM (ms)**	**n**
	MLI1→PC	0.149	0.0273	35	Wilcoxon	2E-10	1.36	0.07	28
	MLI2→PC	−0.053	0.0094	21	Wilcoxon	2E-08	7.82	0.84	15
	MLI1→PC vs MLI2→PC				Wilcoxon	9E-11			
Figure 2l–n	**Group**	**Synchrony (norm.)**	**SEM (norm.)**	**n**	**Test**	**P-Value**			
	MLI1-MLI1	7.99	2.42	7	Wilcoxon	6E-04			
	MLI2-MLI1	1.07	0.05	8	Wilcoxon	0.65			
	MLI1-MLI1 vs MLI2-MLI1				Wilcoxon	0.00031			
Figure S2c	**Group**	**R_i(GOhm)**	**SEM (GOhm)**	**n**	**Test**	**P-Value**			
	MLI1	0.345	0.016	81					
	MLI2	0.849	0.043	63					
	MLI1 vs MLI2				Wilcoxon	3E-10			
Figure S2d	**Group**	**I_h(pA)**	**SEM (pA)**	**n**	**Test**	**P-Value**			

Figure	Group	ΔPostsynaptic Conductance (pS)	SEM (pS)	n	Test	P-Value	Latency (ms)	SEM (ms)	n
	MLI1	17.3	0.8	81					
	MLI2	29.0	1.4	63					
	MLI1 vs MLI2				Wilcoxon	9E-10			
Figure S2h	**Group**	**τ_2(ms)**	**SEM (ms)**	**n**	**Test**	**P-Value**			
	MLI1	6.1	0.3	81					
	MLI2	24.7	2.3	63					
	MLI1 vs MLI2				Wilcoxon	3E-10			

R_i=input resistance. I_h=hyperpolarization-evoked current. τ_2=action potential decay time constant. SEM=standard error of the mean.

Key resources table

REAGENT or RESOURCE	SOURCE	IDENTIFIER
Antibodies		
Chicken polyclonal anti-GFP	Abcam	Cat# ab13970, RRID:AB_300798
Goat anti-chicken Alexa Fluor 488	Abcam	Cat# ab150169, RRID:AB_2636803)
Deposited data		
EM dataset	BossDB	https://bossdb.org/project/nguyen_thomas2022
Experimental models: Organisms/strains		
C57/BL6	Charles River	N/A
Tg(Gjd2-EGFP)JM16Gsat/Mmucd	MMRRC	Stock# 030611-UCD, RRID:MMRRC_0306 11-UCD
B6.Cg-Gt(ROSA)26Sor$^{tm14(CAG-tdTomato)Hze}$/J	Jackson Labs	Strain# 007914, RRID:IMSR_JAX:00 7914
Nxph1^{Cre}	this manuscript	N/A
C57/BL6J	Jackson Labs	strain# 000664, RRID:IMSR_JAX:00 0664
CBA/CaJ	Jackson Labs	strain# 000654, RRID:IMSR_JAX:00 0654
B6.Cg-*Kit*$^{tm1(cre)Htng}$/J (“c-kitIRES-Cre”)	J. Christie Lab (https://www.cerebellumlab.org/)	RRID:IMSR_JAX:03 2923
Software and algorithms		
Igor Pro 8	Wavemetrics	https://www.wavemetrics.com/
MATLAB R2022a	MathWorks	https://www.mathworks.com/products/matlab.html
MATLAB R2019b	MathWorks	https://www.mathworks.com/products/matlab.html
ImageJ/FIJI	NIH	https://fiji.sc/
MD-Seg front-end	GitHub	https://github.com/htem/neuroglancer_mdseg/tree/segway_pr_v2
MD-Seg back-end	GitHub	https://github.com/htem/segway.mdseg
Segmentation and synapse prediction scripts	GitHub	https://github.com/htem/segway
SpikeGLX	GitHub	https://billkarsh.github.io/SpikeGLX
Kilosort 2.0	GitHub	https://github.com/cortex-lab/Kilosort
Phy	GitHub	https://github.com/cortex-lab/phy
Phyllum	GitHub	https://github.com/blinklab/Phyllum_public